Research
AI for Process Manufacturing—Article

STROM: A Spatial–Temporal Reduced-Order Model for Zinc Fluidized Bed Roaster Temperature Field Prediction

Yunfeng Zhang [a], Chunhua Yang [a], Keke Huang [a,*], Tingwen Huang [b], Weihua Gui [a]

[a] School of Automation, Central South University, Changsha 410083, China
[b] Department of Science Program, Texas A&M University at Qatar, Doha 10587, Qatar

ARTICLE INFO

ABSTRACT

With the intelligent transformation of process manufacturing, accurate and comprehensive perception information is fundamental for application of artificial intelligence methods. In zinc smelting, the fluidized bed roaster is a key piece of large-scale equipment and plays a critical role in the manufacturing industry; its internal temperature field directly determines the quality of zinc calcine and other related products. However, due to its vast spatial dimensions, the limited observation methods, and the complex multiphase, multifield coupled reaction atmosphere inside it, accurately and timely perceiving its temperature field remains a significant challenge. To address these challenges, a spatial–temporal reduced-order model (STROM) is proposed, which can realize fast and accurate temperature field perception based on sparse observation data. Specifically, to address the difficulty in matching the initial physical field with the sparse observation data, an initial field construction based on data assimilation (IFC-DA) method is proposed to ensure that the initial conditions of the model can be matched with the actual operation state, which provides a basis for constructing a high-precision computational fluid dynamics (CFD) model. Then, to address the high simulation cost of high-precision CFD models under full working conditions, a high uniformity (HU)-orthogonal test design (OTD) method with the centered L_2 deviation is innovatively proposed to ensure high information coverage of the temperature field dataset under typical working conditions in terms of multiple factors and levels of the component, feed, and blast parameters. Finally, to address the difficulty in real-time and accurate temperature field prediction, considering the spatial correlation between the observed temperature and the temperature field, as well as the dynamic correlation of the observed temperature in the time dimension, a spatial–temporal predictive model (STPM) is established, which realizes rapid prediction of the temperature field through sparse observation data. To verify the accuracy and validity of the proposed method, CFD model validation and reduced-order model prediction experiments are designed, and the results show that the proposed method can realize high-precision and fast prediction of the roaster temperature field under different working conditions through sparse observation data. Compared with the CFD model, the prediction root-mean-square error (RMSE) of STROM is less than 0.038, and the computational efficiency is improved by 3.4184×10^4 times. In particular, STROM also has a good prediction ability for unmodeled conditions, with a prediction RMSE of less than 0.1089.

© 2025 THE AUTHORS. Published by Elsevier LTD on behalf of Chinese Academy of Engineering and Higher Education Press Limited Company. This is an open access article under the CC BY license (http://creativecommons.org/licenses/by/4.0/).

1. Introduction

Process manufacturing is a vital component of modern industry and plays a significant role in the national economy. Accurate perception of the operating status is crucial in process manufacturing, as it provides essential data for process monitoring and control [1,2]. In the past, single perception methods struggled to provide comprehensive information. However, with the advent of new technologies, particularly those driven by artificial intelligence (AI), many advanced intelligent perception methods have been developed for process manufacturing. Zinc smelting is a typical process in the manufacturing industry, and the fluidized bed roaster is a key piece of equipment for zinc smelting. The internal temperature field of the roaster directly determines the quality of zinc calcine (ZnO) and other products. A suitable temperature field

* Corresponding author.
E-mail address: huangkeke@csu.edu.cn (K. Huang).

can promote the conversion of zinc sulfate to zinc oxide, thus improving the quality of zinc calcine. However, a local high-temperature field will lead to dissolution of silicate, which will reduce the purity of zinc calcine and cause a sintering fault. Therefore, perceiving the temperature field in the roaster is essential to improve the quality of zinc smelting [3,4]. Since the roaster is a piece of reaction equipment with a large internal space and complex reaction conditions, only a few sensors can be deployed, resulting in restricted means of observation. Moreover, the multi-field flow–solid heterogeneous coupled reaction atmosphere, including the velocity, temperature, and concentration, is affected by the working condition parameters, such as the feed speed, blast speed, and material components, making accurate perception of the atmosphere difficult [5,6].

With the development of computer simulation technology and the increasing computational power, numerical simulation has become an effective and low-cost technique to understand the reaction atmosphere inside a roaster, and it can provide detailed information on the fluid flow, heat transfer, mass transfer, and chemical reactions [7]. The reaction atmosphere inside a roaster is a typical dense gas–solid multiphase flow, and the numerical simulation methods for this reaction atmosphere mainly include two types: the Eulerian–Lagrangian model based on the dynamics of discrete particles and the Eulerian–Eulerian model based on a particle pseudo-fluid. The Eulerian–Lagrangian model treats the gas phase as a continuous phase, and a system of equations is established to solve it under the Eulerian coordinate system. For the particle phase, the trajectory of each discrete particle in the flow field is tracked on the basis of Newton's laws of mechanics in the Lagrangian coordinate system, and the energy and chemical reaction processes are coupled to obtain the particle motion, temperature, and composition parameters [8]. To solve the problem of inaccurate simulation of the fluidized bed under the assumption of a homogeneous particle size, Wu et al. [9] constructed an oxygenated circulating fluidized bed combustion model based on the dense discrete phase simulation method under the Eulerian–Lagrangian framework to achieve accurate simulation of the fluidized bed roaster, and the simulation results were consistent with the experimental data. To address the unclear product mechanism of the fluidized bed under different working conditions, Hu et al. [10] proposed a simulation method integrating coarse-grained computational fluid dynamics (CFD) and discrete element analysis to model the fluidized bed gasifier, resolving the mechanisms of the influence of different operating parameters on the gasification of bubbling fluidized bed coal. Due to measurement difficulties, the gas flow distribution and particle dynamics mechanism are complex to analyze. To solve this, Liu et al. [11] applied the CFD-discrete element method (DEM) to establish a fluid dynamics model of a fluidized bed and explore the pressure influence mechanism on the fluidization characteristics. However, as more particles are tracked, the computational cost considerably increases, limiting the application of such methods to model industrial-scale reactors.

The Eulerian–Eulerian model treats the particle phase as a pseudo-fluid with the characteristics of a continuous medium and interpenetration with the gas phase. The continuity and momentum equations including the gas and particle phases are established in the Eulerian coordinate system and closed based on molecular and particle dynamics theories, and the critical gas and particle phase flow parameters are obtained, which can realize industrial-scale multiphase flow simulation with a low computational cost [12,13]. To address the unclear mechanism of the influence of fluidizers on the flow characteristics of particles in liquid–solid fluidized beds, Pang et al. [14] numerically simulated the flow behavior of particles and power-law fluids in fluidized beds by using the two-fluid model and kinetic theory of granular flow

and resolved the influence mechanism of the flow behavior indexes and consistency coefficients on the nonuniformity of particles. Due to the significant computational demands in simulating industrial-scale fluidized beds, precise modeling is challenging. To solve this problem, Dash et al. [15] considered four particle phases and one gas phase to establish a multiphase Eulerian–Eulerian model for roasters, and the simulation results matched the actual data of a plant well. To address the problem that the three-dimensional (3D) integrated operation mechanism of coal combustion in a circulating fluidized bed system is not precise, Wu et al. [16] established a 3D integrated model of coal combustion in a circulating fluidized bed under an air environment by using the Eulerian–Eulerian method based on a 50 kW (thermal) circulating fluidized bed combustion chamber, and the simulation results well matched the experimental data, which provided a complete physical image including the flow, temperature, and gas composition.

More recently, related improvements have been made to apply CFD models in practice [17–19] while ensuring the accuracy of the CFD model, reducing the cost of tests, and enhancing the efficiency of the model calculation. To achieve accurate simulation of the greenhouse cooling performance, Saberian and Sajadiye [20] applied meteorological simulation data to set the initial conditions of the CFD model and verified the accuracy of the CFD simulation through physical experiments. To reduce the high computational cost of a high-fidelity 3D gasifier simulation, Yu et al. [21] adopted one-dimensional CFD-DEM simulation results as the accurate initial conditions of the 3D simulation, which significantly shortened the time required for the model to reach the steady state and realized accurate simulation of the gasifier. Although the above method can improve the model accuracy, the simulation cost of comprehensive high-precision CFD simulations under full working conditions is high. Therefore, to reduce the cost, a reasonable test design to obtain typical working condition data is required. To solve the problems that the temperature field of a tubular reactor is affected by multiple heaters and that comprehensive simulation is costly, Xie et al. [22] applied an orthogonal experimental design method to obtain the data of typical working conditions, which were used to reduce the number of experiments from an exponential level to a linear level. The complex reactions in a fluidized bed make obtaining a dataset that adequately covers its operating characteristics difficult. To solve this problem, Du et al. [23] combined a neural network with an energy-minimization multiscale (EMMS) drag model for parameterization to establish a complete fluidized bed simulation scheme to obtain typical operating data under the influence of gas properties and operating parameters. However, the above methods can only reduce simulation costs in the offline stage. High-precision CFD models usually take a long time to solve, making meeting the real-time requirements of online applications challenging. With the accumulation of simulation data providing a new path for fast and accurate prediction of the temperature field, data-driven reduced-order prediction methods have been proposed [24,25]. When the process mechanism is unknown, establishing an accurate model is difficult. To solve this problem, Qing et al. [26] proposed a spatial–temporal coupling model reduction framework that combines an encoder–decoder network with a recurrent neural network, achieving rapid reactor temperature field prediction. Since the complexity of high-dimensional models limits their application, Lorenzetti et al. [27] proposed a reduced-order model predictive control method to solve the optimal control problem of high-dimensional linear systems, achieving an efficient solution that satisfies robust constraints and stability requirements.

The above methods can achieve fast and accurate prediction of temperature fields to some extent. However, due to the large space of a roaster, limited observation methods, and complex reaction atmosphere, rapidly and accurately predicting the roaster

temperature field via the above methods is difficult. In summary, there are three problems: ① Matching the initial physical field of the model with the actual sparse observation data is difficult; ② the roaster temperature field has multiple working conditions, with a high computational cost for comprehensive simulation; and ③ quickly and accurately predicting the roaster temperature field based on the sparse observation data is difficult. To solve these issues, a spatial–temporal reduced-order model (STROM) is proposed, which can quickly and accurately predict the temperature field based on sparse temperature observation data. First, to address the difficulty in matching the initial physical field of the model with sparse observation data, an initial field construction based on data assimilation (IFC-DA) method is proposed, which can reconstruct the initial conditions of the model with high resolution. Then, to reduce the high computational cost of comprehensive simulation of the roaster with multiple working conditions, a high uniformity (HU)-orthogonal test design (OTD) method is proposed, which ensures high information coverage of temperature field datasets for typical working conditions. Finally, to address the difficulty of real-time prediction of the temperature field, considering the spatial and dynamic correlation, a spatial-temporal predictive model (STPM) is proposed, which can realize rapid prediction of the temperature field based on sparse observation data. In summary, the main contributions of this paper are as follows:

- To overcome the difficulty in matching the initial physical field of the model with the actual sparse observation data, an IFC-DA method is proposed to realize high-precision and high-resolution reconstruction of the initial field.
- To reduce the high computational cost of roaster temperature field simulations under full working conditions, an HU-OTD method in which the centered L_2 deviation is introduced is innovatively proposed, which can obtain typical working condition data with sufficient coverage of parameter ranges.
- To achieve real-time and accurate prediction of the roaster temperature field, an STPM is proposed, which can realize fast and accurate prediction of the entire temperature field based on sparse temperature observation data and improve the computational efficiency by 3.4184×10^4 times compared with that of numerical simulation methods.
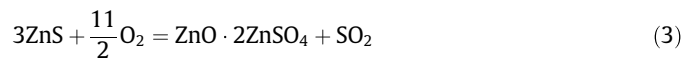
The remainder of this paper is structured as follows. In Section 2, the operating characteristics of the roaster and the difficulties faced in real-time accurate prediction are analyzed. In Section 3, the framework of STROM is presented. In Section 4, the superiority of the proposed method is verified through extensive experiments. Concluding remarks are given in Section 5.

2. Process analysis

This section describes the operating mechanism of a roaster and analyzes the difficulties faced in quickly and accurately predicting the temperature field of the roaster from the perspective of practical application.

2.1. Process description

As shown in Fig. 1(a), the roaster mainly contains five units: the feeding unit, blower unit, roaster furnace, flue gas unit, and calcine unit. The feeding unit is used to throw the zinc concentrate, which is mainly composed of ZnS and Si, into the roaster. The blower unit supplies the roaster with air. The flue gas unit exhausts and recovers SO_2 gas. The calcine unit transports zinc calcine (ZnO) for the subsequent leaching process. The main reactions occurring in the roaster are as follows:

$$ZnS + \frac{3}{2}O_2 = ZnO + SO_2 \tag{1}$$

$$ZnS + 2O_2 = ZnSO_4 \tag{2}$$

$$3ZnS + \frac{11}{2}O_2 = ZnO \cdot 2ZnSO_4 + SO_2 \tag{3}$$

where reaction (1) is the primary reaction that produces zinc calcine, whereas reactions (2) and (3) produce impurities, affecting the quality of zinc calcine.

The roaster has a coupled reaction atmosphere of flow, concentration, and temperature fields, as shown in Fig. 1(b). First, the blast speed drives the flow field to form a velocity distribution inside the roaster, which affects the concentration and temperature distributions through mass and heat transfer of the fluid. The zinc concentrate is then ejected from the feeding unit and suspended by the fluid to form a fluidized reaction atmosphere, which enables the oxygen and the ore to be in full contact to carry out the redox reaction. In the fluidized roaster, the ore particles are affected by their own gravity and fluid traction, resulting in a concentration field distribution due to the different particle sizes and velocity distributions. Finally, the zinc concentrate and oxygen undergo a chemical reaction, as shown in reactions (1)–(3). This reaction is exothermic, and locations with high ore concentrations release more heat, resulting in a temperature distribution. Heat is transferred from high- to low-temperature locations through thermal diffusion and convection, forming a temperature field.

The temperature field in the roaster determines the quality of the zinc calcine product. On the one hand, from the thermodynamic analysis of the Zn–S–O chemical reaction, a higher temperature promotes decomposition of $ZnSO_4$, which produces more ZnO (zinc calcine). On the other hand, there will be silicate impurities in the product. According to an analysis of the physical properties of impurities, silicate has a low melting point, and a high temperature will cause it to melt, thereby reducing the purity of the zinc calcine. Therefore, considering both aspects, the temperature field of the roaster must be perceived in real time to stabilize the temperature within a specific range and ensure the purity of the zinc calcine product.

2.2. Challenges in temperature field prediction

The internal reaction mechanism of the roaster is complex, and the working conditions frequently fluctuate with changes in the inlet raw material. Additionally, owing to the large size of the fluidized bed roaster, the high temperature in the roaster, and the limited observation methods, rapid and accurate prediction of the temperature field faces three challenges as follows.

2.2.1. Difficultly matching the initial physical field with sparse observation data

CFD simulation is usually applied to obtain the internal reaction atmosphere of a roaster. The simulation accuracy depends on accurate initial conditions. Even if there is a slight deviation, significant simulation errors will occur after multiple simulation iterations. However, owing to the limitations of observations, only low-resolution initial physical fields can be obtained, as shown in Fig. 2(a). Compared with the actual initial physical field, the details deviate. In addition, only sparse observation data can be collected, as shown in Fig. 2(b). Therefore, the first challenge that needs to be solved is how to reconstruct the high-precision and high-resolution physical field based on the low-resolution initial physical field and sparse observation data.
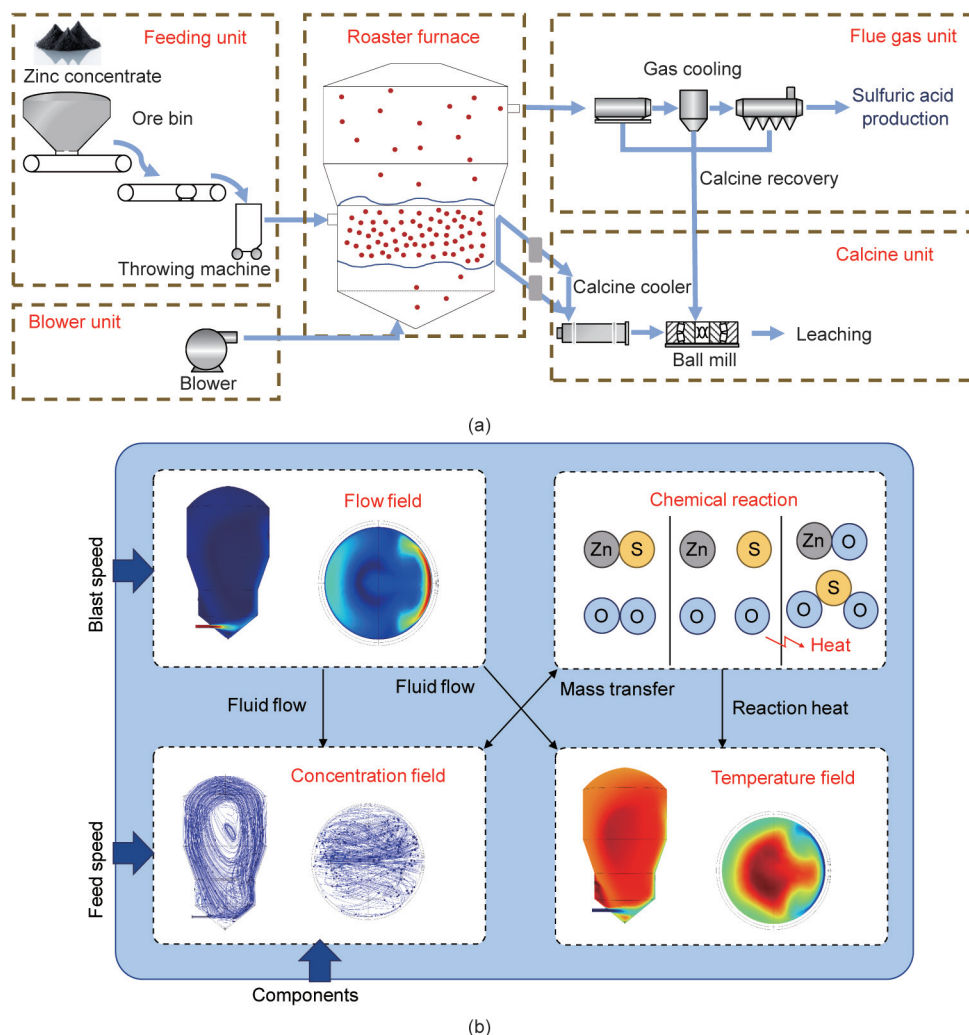
(a)

(b)

Fig. 1. Process analysis of a fluidized bed roaster. (a) Operating mechanism; (b) field coupling relationship.
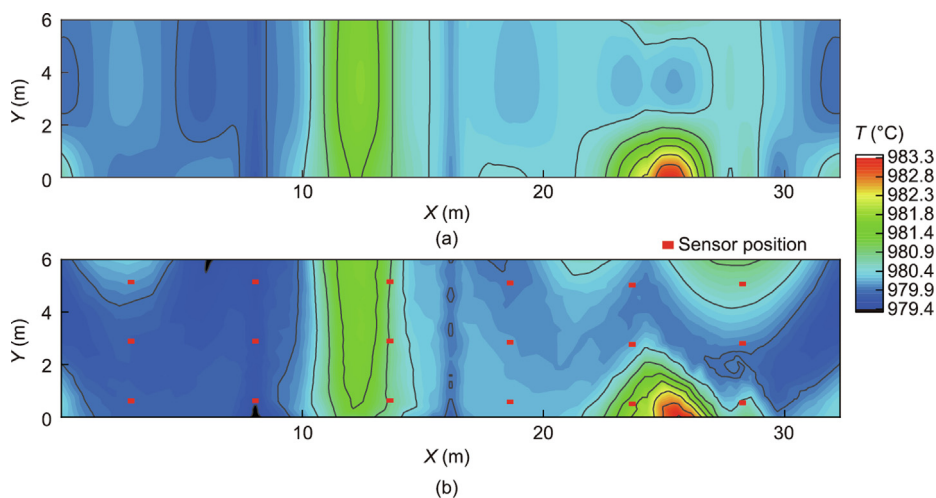

Fig. 2. Initial physical field: (a) low resolution (0.1 m × 0.1 m) and (b) real (0.05 m × 0.05 m).

2.2.2. High cost of simulations for full working conditions

The reaction atmosphere in the roaster is affected by factors such as the feed speed, blast speed, and components, and there are multiple working conditions. Extensive simulations are usually required for comprehensive consideration, and high-precision CFD simulation costs are high. The OTD method is applied to obtain typical working conditions, which can reduce the number of experiments from $O(n_l^{n_f})$ to $O(n_l n_f)$ (where $O(\cdot)$ is time complexity, n_l is

the number of levels, and n_f is the number of factors), significantly reducing the cost. However, the OTD method does not consider the uniformity of the parameter distribution and cannot fully cover the parameter range. Therefore, the second challenge is how to design experiments to obtain data of typical conditions with low simulation costs and to fully cover the operating characteristics within the parameter range.

2.2.3. Difficulty accurately predicting the temperature field in real time

The roaster has a large internal space, with a radius of approximately 6.9 m and a height of approximately 34 m. However, owing to the complex internal reaction environment, only a few sensors can be deployed on the reactor wall, and the monitoring methods are limited, making perception of the reaction atmosphere difficult. Moreover, CFD models usually require hours of simulation time to simulate changes in the reaction atmosphere, which makes CFD simulations difficult to apply in real applications. Therefore, the third challenge is how to use sparse observation data to quickly and accurately predict the temperature field of the roaster.

3. Spatial–temporal reduced-order model

This section presents the STROM in detail, including CFD modeling, IFC-DA, HU-OTD, and STPM. The overall framework of the method is shown in Fig. 3.

3.1. CFD modeling

Computer simulation is used to model the reaction atmosphere inside the roaster. It consists of two steps: mathematical model construction and model solution. Moreover, considering the complex operation process of the roaster, to ensure the success of the calculation, the following assumptions are made for the model:

- The gas and particle phase fluids inside the roaster are continuous media and interpenetrate each other.

- According to the analysis of the relationship between the fields in the roaster, the order of influence of the physical fields in the roaster is the flow, concentration, and then temperature fields.
- The forces between the gas and solid phases are considered only for the effect of trailing forces, and other smaller forces are not considered.

3.1.1. Mathematical model construction

The reaction atmosphere inside the roaster is a dense gas–solid multiphase fluid. Two methods are usually applied to describe the atmosphere: the Eulerian–Lagrangian and Eulerian–Eulerian methods. Both methods treat the gas phase in the same way: as a continuous fluid. The Eulerian–Lagrangian method tracks each solid particle for the solid phase in the Lagrangian coordinate system. As the number of particles increases, because the model calculation complexity is $O(N^2)$, where N is the number of particles, meeting the high-precision modeling requirements for large-scale roasters becomes challenging. The Eulerian–Eulerian method treats the solid phase as a continuous fluid, greatly reducing the calculation amount. Therefore, under the assumption that the gas and particle phase fluids inside the roaster are continuous media that permeate each other, the Eulerian–Eulerian method is applied to model the reaction atmosphere inside the roaster. The STROM improves the implementation of the Eulerian–Eulerian framework in two main aspects: model solution and initial condition acquisition. The STROM uses a sequential calculation method to solve the Eulerian–Eulerian framework according to the influence relationship and sequence of the physical fields in the roaster. In addition, STROM uses 3D variation assimilation to combine simulation results and sparse parameter data to obtain accurate initial conditions for the Eulerian–Eulerian framework. The application of the Eulerian–Eulerian model requires specification of the governing equations, including those for the continuity, momentum, energy, component, and chemical reaction models [28,29], which are described below.
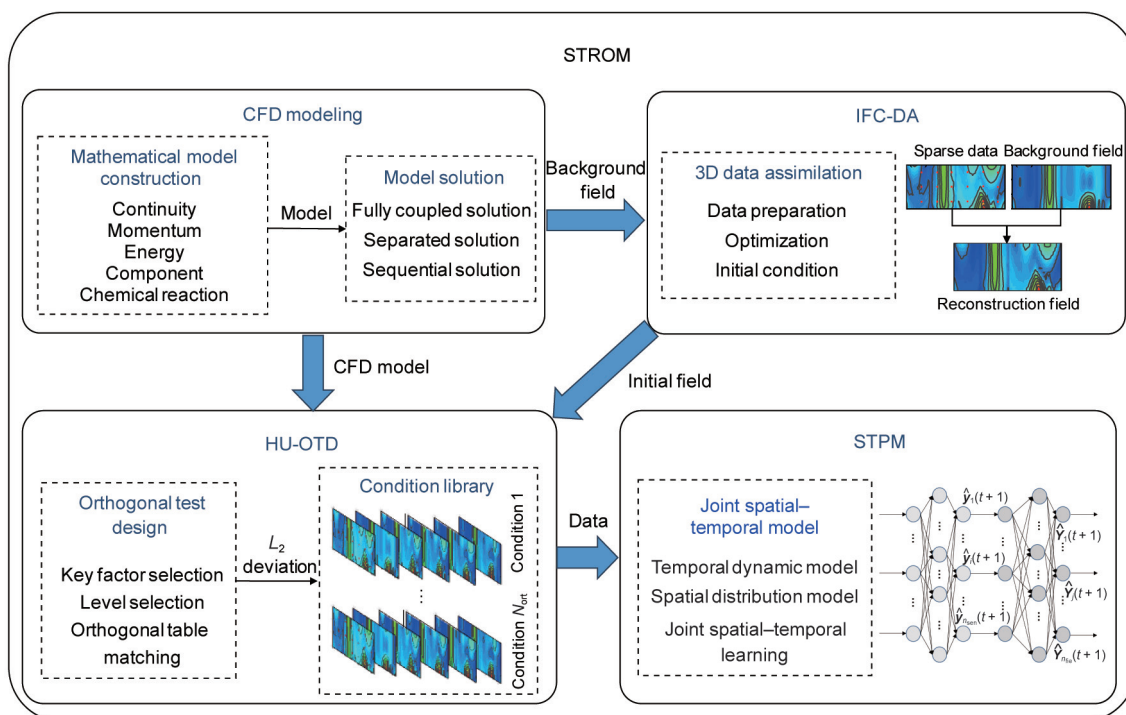

Fig. 3. Framework of STROM.

Continuity equation: The continuity equation is used to describe the conservation of mass and contains the mass change rate, the spatial variation in mass due to convection, and the source term for the mass transfer between phases. The temporal and spatial gradients for the gas and solid phases are defined as follows:

$$\frac{\partial}{\partial t}\left(\alpha_g \rho_g\right) + \nabla \cdot \left(\alpha_g \rho_g \boldsymbol{u}_g\right) = S_{gs} \tag{4}$$

$$\frac{\partial}{\partial t}\left(\alpha_s \rho_s\right) + \nabla \cdot \left(\alpha_s \rho_s \boldsymbol{u}_s\right) = S_{sg} \tag{5}$$

where α, ρ, t, and $\boldsymbol{u}$ are the volume fraction, the density of each phase, time, and the velocity, respectively. ∇ is gradient operator. The subscripts g and s represent the gas and solid phases, respectively. S represents the mass transfer between the gas phase and the solid phase, which satisfies the following relationship:

$$S_{gs} = -S_{sg} \tag{6}$$

In the Eulerian–Eulerian model, the gas and solid phases are both considered to be fluids, which together constitute the flow medium. Therefore, the volume fractions of the two phases satisfy the following relationship:

$$\alpha_g + \alpha_s = 1 \tag{7}$$

Momentum equation: The momentum equation reflects that the momentum change rate is affected by three factors: the change in momentum with space due to convection, external forces, and the change in momentum due to mass transfer between phases. The external forces include pressure, viscous stress, gravity, and phase drag. The momentum conservation equations for the gas and solid phases are as follows:

$$\frac{\partial}{\partial t}\left(\alpha_g \rho_g \boldsymbol{u}_g\right) + \nabla \cdot \left(\alpha_g \rho_g \boldsymbol{u}_g \boldsymbol{u}_g\right) = -\alpha_g \nabla P_g + \nabla \alpha_g \cdot \boldsymbol{\tau}_g + \alpha_g \rho_g g$$
$$+ \beta\left(\boldsymbol{u}_s - \boldsymbol{u}_g\right) + S_{gs}\boldsymbol{u}_g \tag{8}$$

$$\frac{\partial}{\partial t}\left(\alpha_s \rho_s \boldsymbol{u}_s\right) + \nabla \cdot \left(\alpha_s \rho_s \boldsymbol{u}_s \boldsymbol{u}_s\right) = -\alpha_s \nabla P_s + \nabla \alpha_s \cdot \boldsymbol{\tau}_s + \alpha_s \rho_s g$$
$$+ \beta\left(\boldsymbol{u}_g - \boldsymbol{u}_s\right) + S_{sg}\boldsymbol{u}_s \tag{9}$$

where P is the static pressure, $\boldsymbol{\tau}$ is the viscous stress tensor, g is the gravitational acceleration, and β is the drag coefficient between the gas and solid phases. In the above gas–solid momentum conservation model, the stress tensor needs to be closed as follows:

$$\boldsymbol{\tau}_g = \mu_g\left[\nabla \boldsymbol{u}_g + \left(\nabla \boldsymbol{u}_g\right)^T\right] - \frac{2}{3}\mu_g\left(\nabla \boldsymbol{u}_g\right) \tag{10}$$

$$\boldsymbol{\tau}_s = \mu_s\left[\nabla \boldsymbol{u}_s + \left(\nabla \boldsymbol{u}_s\right)^T\right] - \frac{2}{3}\mu_s\left(\nabla \boldsymbol{u}_s\right) + \lambda_s \nabla \boldsymbol{u}_s \tag{11}$$

where μ is the shear viscosity and λ_s is the bulk viscosity of the solid phase.

Energy equation: The energy equation reflects that the energy change rate is affected by four factors: convective heat transfer, diffusive heat transfer, external heat sources, and the energy change caused by phase mass change. The energy equations for the gas and solid phases are as follows:

$$\frac{\partial}{\partial t}\left(\alpha_g \rho_g H_g\right) + \nabla \cdot \left(\alpha_g \rho_g \boldsymbol{u}_g H_g\right) = \nabla(k_g \nabla T_g) + Q_{gs} + S_{gs}H \tag{12}$$

$$\frac{\partial}{\partial t}\left(\alpha_s \rho_s H_s\right) + \nabla \cdot \left(\alpha_s \rho_s \boldsymbol{u}_s H_s\right) = \nabla(k_s \nabla T_s) + Q_{sg} + S_{sg}H \tag{13}$$

where H, T, and k represent the enthalpy, temperature, and thermal conductivity, respectively. Q is the interphase heat transfer between the gas and solid phases, which is calculated as follows:

$$Q_{sg} = h_{sg}\left(T_s - T_g\right) = -Q_{gs} \tag{14}$$

$$H = \sum_{a=1}^{n_{spe}} Y_a H_a \tag{15}$$

where h is convective heat transfer, n_{spe} is the number of components, and Y_a is the mass fraction of the ath component. The enthalpy (H_a) of the ath component is calculated as follows:

$$H_a = \int_{T_0}^{T} C_{p,a} dT + \nabla H_{f,a} \tag{16}$$

where T_0, $C_{p,a}$, and $\nabla H_{f,a}$ are the reference temperature, heat capacity of each component at constant pressure, and standard generation enthalpy of the ath component, respectively.

Component equation: The component equation is used to describe the conservation of mass for each component. This is expressed as the change in the mass of component a, which is affected by convective transfer, diffusive transfer, and the reaction source term. The component transport equations for the gas and solid phases are as follows:

$$\frac{\partial}{\partial t}\left(\alpha_g \rho_g Y_{a,g}\right) + \nabla \cdot \left(\alpha_g \rho_g \boldsymbol{u}_g Y_{a,g}\right) = -\nabla \alpha_g \bar{J}_{a,g} + r_{a,g} \tag{17}$$

$$\frac{\partial}{\partial t}\left(\alpha_s \rho_s Y_{a,s}\right) + \nabla \cdot \left(\alpha_s \rho_s \boldsymbol{u}_s Y_{a,s}\right) = -\nabla \alpha_s \bar{J}_{a,s} + r_{a,s} \tag{18}$$

where $Y_{a,g}$ and $Y_{a,s}$ denote the mass fractions of the ath component in the gas and solid phases, respectively; $\bar{J}$ is the diffusion phase of the component equation; and $r_{a,g}$ and $r_{a,s}$ denote the chemical reaction rates of the ath component in the gas and solid phases, respectively.

Chemical reaction: Reaction (1) is an exothermic reaction that mainly affects the temperature of the roaster. Therefore, the state of reaction (1) is studied, and the Arrhenius formula is used to express the reaction rate (r) as follows:

$$r = k_{rea} \prod_{b=1}^{n_{rea}} C_b \Delta H \tag{19}$$

$$k_{rea} = A \exp\left(-\frac{E}{RT}\right) \tag{20}$$

where C_b, ΔH, n_{rea}, k_{rea}, A, E, and R represent the concentration of the bth reactant, reaction enthalpy, the number of reactant species, rate constant, pre-exponential factor, chemical reaction activation energy, and molar gas constant, respectively.

3.1.2. Model solution

After the partial differential equation (PDE) model of the roaster has been established, calculations must be performed to obtain the states of its internal physical fields. There are three main methods for solving multiphysics field PDEs: fully coupled, separated, and sequential solution methods. In the fully coupled solution method, all the physical fields must be considered in each computational step, forming a large set of equations for iterative computation. Although the computational accuracy is high, the computational amount is significant, and the model cannot easily converge under working conditions in which the boundary conditions fluctuate. However, in the actual process, feeding and blowing operations are frequently performed, making this calculation method inapplicable. The separated solution method also considers all physical fields in each computational step, except that each physical field is separately computed and does not form a set of equations containing all physical fields, simplifying the Jacobian matrix during iterative computation. However, this method cannot easily

converge. The sequential solution method solves the following physical field based on the solution results of one physical field after it converges, facilitating convergence of the model. Moreover, according to the analysis of the coupling relationship between the physical fields of the roaster, the flow, concentration, and temperature fields satisfy the sequential influence relationship, so the sequential solution method is applied to solve the model. The solution for each physical field is usually obtained by using spatial and temporal discretization to obtain a recursive form of the PDE.

The temperature field is taken as an example to describe the calculation process. Consider the physical field state as $T = T(x, t)$, which satisfies the following PDE:

$$\rho C_p T_t + \nabla \cdot (-k\nabla T) = g(T, x, t) \text{ in } \Omega \tag{21}$$

$$T(x, 0) = T_0; \; -(k\nabla T) \cdot \boldsymbol{n} = q \text{ on } \partial\Omega \tag{22}$$

where C_p, T_t, $g(T, x, t)$, x, Ω, $\boldsymbol{n}$, q, and $\partial\Omega$ represent heat capacity, partial derivative of temperature with respect to time, the heat source, spatial location, the entire model domain, the unit normal vector extending outward from the boundary, the heat exchange heat source, and boundaries, respectively. By multiplying Eq. (21) by the trial function φ and integrating over domain Ω, this equation can be converted as follows:

$$\int_\Omega [\rho C_p T_t + \nabla \cdot (-k\nabla T)]\varphi dV = \int_\Omega g(T, x, t)\varphi dV \tag{23}$$

where V denotes volume. By applying the first Green's formula, Eq. (23) can be transformed as follows:

$$\int_\Omega (\rho C_p T_t \varphi + k\nabla T \cdot \nabla\varphi)dV + \int_{\partial\Omega} (-k\nabla T) \cdot \boldsymbol{n}\varphi dS$$
$$= \int_\Omega g(T, x, t)\varphi dV \tag{24}$$

The trial function $\varphi \in \{\psi_1, \psi_2, \ldots, \psi_{N_{spa}}\}$ consists of N_{spa} spatial basis functions, which cover the entire calculation domain. ψ is the spatial basis function. The basis functions satisfy the following relationship:

$$\psi_c(x_d) = \begin{cases} 1, c = d \\ 0, c \neq d \end{cases} \tag{25}$$

The entire physical field state can be represented by the spatial basis functions and the corresponding time coefficients as follows:

$$T(x, t) = \sum_{c=1}^{N_{spa}} T_c(t)\psi_c(x) \tag{26}$$

where $T_c(t)$ denote the cth time coefficient. For each trial function ψ_c, $c = 1, \ldots, N_{spa}$, Eq. (24) can be expressed as follows:

$$\sum_{c=1}^{N_{spa}} \rho C_p \frac{\partial T_c(t)}{\partial t} \int_\Omega \psi_c\psi_d dV + \sum_{c=1}^{N_{spa}} T_d(t) \int_\Omega k\nabla\psi_c \cdot \nabla\psi_d dV$$
$$+ \int_{\partial\Omega} (-kT_c(t)\nabla\psi_d \cdot \boldsymbol{n})\psi_d dS = -\int_{\partial\Omega} g\left(\sum_{c=1}^{N_{spa}} T_c(t)\psi_d, x, t\right)dV \tag{27}$$

Eq. (27) is discretized in the time dimension using the differential approximation method as follows:

$$\frac{\partial T_c(t)}{\partial t} \approx \frac{T_c(t + \Delta t) - T_c(t)}{\Delta t} \tag{28}$$

Then, Eq. (27) can be converted as follows:

$$\sum_{c=1}^{N_{spa}} \rho C_p \frac{T_c(t + \Delta t) - T_c(t)}{\Delta t} \int_\Omega \psi_c\psi_d dV + \sum_{c=1}^{N_{spa}} T_i(t) \int_\Omega k\nabla\psi_c$$
$$\cdot \nabla\psi_d dV + \int_{\partial\Omega} (-kT_c(t)\nabla\psi_c \cdot \boldsymbol{n})\psi_d dS$$
$$= -\int_{\partial\Omega} g\left(\sum_{c=1}^{N_{spa}} T_c(t)\psi_c, x, t\right)dV \tag{29}$$

In Eq. (29), $T_c(t + \Delta t)$ needs to be solved, and the rest of the variables and parameters are known. The result of $T_c(t + \Delta t)$ can be used for the calculation in the next time step. In this way, according to the initial and boundary conditions of Eq. (22), the solution of Eq. (29) can be recursively obtained at any time $t + \Delta t$.

3.2. Initial field construction based on data assimilation

The high calculation cost of the CFD model makes it difficult to apply in practice, so a reduced-order model is required. To achieve accurate simulation of the roaster temperature field by the reduced-order model, an accurate CFD model is needed to provide the training dataset. The accuracy of the CFD simulation depends on the initial conditions. Large simulation errors will accumulate after iterative calculations if there is a deviation from the initial physical field. However, only low-resolution initial physical fields and sparse observation data can be obtained due to limited observations, making reconstruction of high-resolution initial physical fields difficult. To solve this problem, the IFC-DA method is proposed based on 3D variational data assimilation theory. This method can interpolate sparse observations to grid points under dynamic constraints to improve the accuracy of the initial physical field. The framework of IFC-DA is shown in Fig. 4, and the specific steps are as follows:

The initial observed temperature data $y_o \in \mathbf{R}^{n' \times m'}$, where n' represents the number of observation locations and m' represents the number of observation states, can be expressed as follows:

$$y_o = H_m(x_r) + \varepsilon \tag{30}$$

where $x_r \in \mathbf{R}^{N_{gri} \times M}$ represents the real physical field, N_{gri} represents the number of model grids, and M represents the number of model states. $H_m(\cdot)$ is the observation operator, which converts the model space to the observation space. ε is the observation error, which is assumed to obey an unbiased Gaussian distribution, and $E\{\varepsilon\} = 0$, $E\{\varepsilon^T \varepsilon\} = \boldsymbol{B}$ (where $E\{\cdot\}$ represents mean calculation and $\boldsymbol{B}$ denotes the covariance matrix of ε).

$$p(y_{est} = y_o | x_{est} = x_r) = p(\varepsilon = y_o - H_m(x_{est}))$$
$$= \frac{1}{\sqrt{2\pi|\boldsymbol{B}|}}$$
$$\times \exp\left\{-\frac{1}{2}[y_o - H_m(x_{est})]^T \boldsymbol{B}^{-1}[y_o - H_m(x_{est})]\right\} \tag{31}$$

where x_{est} is estimation physical field and y_{est} is the estimation of observation data. $p(\cdot)$ is the probability. The background field $x_b \in \mathbf{R}^{n_{gri} \times m}$ is the calculation of the real physical field x_r, where $n_{gri} \leq N_{gri}$ and $m \leq M$, and it can be expressed as follows:

$$x_b = H_i(x_r) + \zeta \tag{32}$$

where ζ is the background error and $H_i(\cdot)$ is the interpolation function, which interpolates the real physical field to the grids of the background field so that both have the same resolution. Additionally, assume that ζ obeys an unbiased Gaussian distribution and that $E\{\zeta\} = 0$, $E\{\zeta^T \zeta\} = \boldsymbol{O}$ (where $\boldsymbol{O}$ denotes the covariance matrix of ζ).
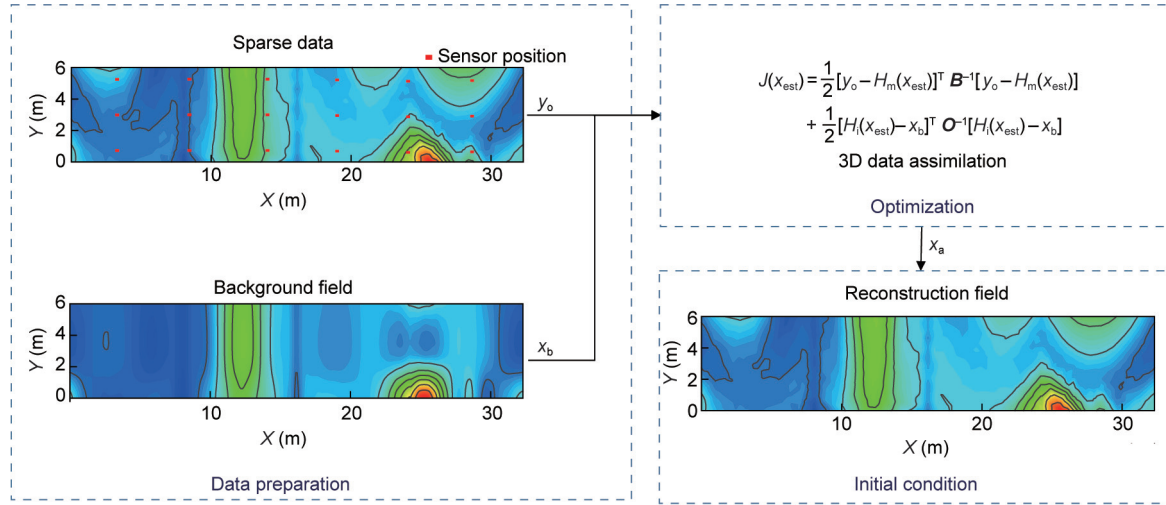
Fig. 4. Framework of IFC-DA. All the variables are defined in the following text.

$$p(x_{est} = x_r) = p(\zeta = x_b - H_i(x_{est}))$$

$$= \frac{1}{\sqrt{2\pi|\mathbf{O}|}}$$

$$\times \exp\left\{-\frac{1}{2}[H_i(x_{est}) - x_b]^T\mathbf{O}^{-1}[H_i(x_{est}) - x_b]\right\} \quad (33)$$

By combining Eqs. (31) and (33), the following can be obtained:

$$p(x_{est} = x_r|y_{est} = y_o) = \frac{p(y_{est}=y_o|x_{est}=x_r)p(x_{est}=x_r)}{p(y_{est}=y_o)}$$

$$= \frac{\exp\left\{-\frac{1}{2}[y_o - H_m(x_{est})]^T\mathbf{B}^{-1}[y_o - H_m(x_{est})] - \frac{1}{2}[H_i(x_{est}) - x_b]^T\mathbf{O}^{-1}[H_i(x_{est}) - x_b]\right\}}{2\pi p(y_{est}=y_o)\sqrt{|\mathbf{B}||\mathbf{O}|}} \quad (34)$$

Eq. (34) estimates the physical field when the observation data are y_o so that the obtained analytical field $x_a \in \mathbf{R}^{N_{gri} \times M}$ is as close as possible to the actual physical field x_r. Since the observation data are known, $p(y_{est}=y_o)$, that is, the denominator of Eq. (34), is a constant, and the log calculation of Eq. (34) can be obtained as follows:

$$-\ln[p(x_{est} = x_r|y_{est} = y_o)] = \frac{1}{2}[y_o - H_m(x_{est})]^T\mathbf{B}^{-1}[y_o - H_m(x_{est})]$$

$$+\frac{1}{2}[H_i(x_{est}) - x_b]^T\mathbf{O}^{-1}[H_i(x_{est}) - x_b] + \ln\left[2\pi p(y_{est} = y_o)\sqrt{|\mathbf{B}||\mathbf{O}|}\right] \quad (35)$$

The third term on the right side of Eq. (35) is a constant. When Eq. (35) reaches the minimum value, Eq. (34) reaches the maximum value. Therefore, the objective function $J(x)$ can be defined as follows:

$$J(x_{est}) = \frac{1}{2}[y_o - H_m(x_{est})]^T\mathbf{B}^{-1}[y_o - H_m(x_{est})]$$

$$+\frac{1}{2}[H_i(x_{est}) - x_b]^T\mathbf{O}^{-1}[H_i(x_{est}) - x_b] \quad (36)$$

When the objective function reaches the minimum value, the corresponding analysis field x_a is obtained and introduced into the model as the initial condition. The quasi-Newton and conjugate gradient methods can be used to solve the optimization problem of Eq. (36). However, the quasi-Newton method needs to calculate the Hessian matrix in each iteration, and the multiphysics coupling reaction atmosphere in the roaster makes the calculation complicated. In contrast, the conjugate gradient method only requires vector calculations and has a low computational complexity. Therefore, the conjugate gradient method is applied to solve the above optimization problem.

3.3. High uniformity-orthogonal test design

The reduced-order model is a data-driven model whose prediction performance for different operating conditions of the temperature field depends on the completeness of the training dataset. The temperature field of the roaster is affected by many factors, such as the feed speed, blast speed, and components, and each factor has multiple operating levels, causing the roaster to have multiple working conditions. If a comprehensive simulation is performed, the experimental cost will be high. The OTD method, in contrast, has the characteristics of a uniform distribution and unity comparability, which enables the test to fully reflect the characteristics of the object while reducing the experimental cost, and has been proven to be a cost-effective method for modeling multiple working conditions [30]. The OTD method mainly includes key factor selection, level selection, and orthogonal table matching. First, for the roaster temperature field mechanism equation, the factors influencing the system state, such as the heat transfer, chemical reaction, and heat source terms, are analyzed, and n_f key influence factors are extracted. Then, based on the operating range of each factor, combined with the analysis of the mechanisms, the levels of each factor $n_{e,l}$ ($e = 1, \ldots, n_f$) are obtained. Finally, the corresponding orthogonal table is constructed according to the number of factors n_f and levels n_l, and the operating parameters of the typical working conditions are set based on this table. After the above steps, the typical working conditions can be obtained, and the required number of tests (N_{ort}) is calculated as follows:

$$N_{ort} = \sum_{e=1}^{n_f} n_{e,l} - n_f + 1 \quad (37)$$

If the OTD method is not used and a comprehensive test is conducted on n_l levels and n_f factors, the number of tests required (N_{all}) is calculated as follows:

$$N_{all} = \prod_{e=1}^{n_f} n_{e,l} \quad (38)$$

A comparison of Eqs. (37) and (38) reveals that the OTD method can reduce the number of tests from the exponential level to the linear level, effectively reducing test costs.

However, the OTD method loses its uniform distribution properties when the unity comparability of the design is considered, resulting in parameter settings that do not adequately cover the

parameter ranges. Therefore, the centered L_2 deviation (D^2) is introduced to assess the uniformity of the experimental design, which can reflect the uniformity of the orthogonal table under low-dimensional projection and is calculated as follows:

$$D^2(P_{tes}, K) = \int_{\chi^2} K(\boldsymbol{u}_t, \boldsymbol{v}_t) \mathrm{d}(F_p - F_u)(\boldsymbol{u}_t) \mathrm{d}(F_p - F_u)(\boldsymbol{v}_t)$$
$$= \int_{\chi^2} K(\boldsymbol{u}_t, \boldsymbol{v}_t) \mathrm{d}\boldsymbol{u}_t \mathrm{d}\boldsymbol{v}_t - \frac{2}{n_{tes}} \sum_{i=1}^{n_{tes}} \int_{\chi^2} K(\boldsymbol{u}_t, \boldsymbol{x}_{t,i}) \mathrm{d}\boldsymbol{u}_t + \frac{1}{n_{tes}^2} \sum_{i=1}^{n_{tes}} \sum_{s=1}^{n_{tes}} K(\boldsymbol{x}_{t,i}, \boldsymbol{x}_{t,s})$$

(39)

where $\chi = [0,1]^{s_{tes}}$ indicates that the test area is an s_{tes}-dimensional unit hypercube. $P_{tes} = \{\boldsymbol{x}_{t,1}, \ldots, \boldsymbol{x}_{t,n_{tes}}\} \in \mathbf{R}^{n_{tes} \times s_{tes}}$ represents the n_{tes} test points in the test area, and $\forall \boldsymbol{u}_t, \boldsymbol{v}_t \in P_{tes}$. F_p and F_u represent the empirical and uniform distribution functions, respectively. K is the kernel function and is calculated as follows:

$$K(\boldsymbol{u}_t, \boldsymbol{v}_t) = \prod_{j=1}^{s_{tes}} \left(1 + \frac{1}{2}\left|u_{t,j} - \frac{1}{2}\right| + \frac{1}{2}\left|v_{t,j} - \frac{1}{2}\right| - \frac{1}{2}|u_{t,j} - v_{t,j}|\right) \quad (40)$$

where u_t and v_t are the elements of vectors $\boldsymbol{u}_t$ and $\boldsymbol{v}_t$, respectively. By applying Eq. (40) to Eq. (39), the centered L_2 deviation can be calculated as follows:

$$D^2(P_{tes}) = \left[\left(\frac{13}{12}\right)^{s_{tes}} - \frac{2}{n_{tes}} \sum_{i=1}^{n_{tes}} \prod_{j=1}^{s_{tes}} \left(1 + \frac{1}{2}\left|x_{t,ij} - \frac{1}{2}\right| - \frac{1}{2}\left|x_{t,ij} - \frac{1}{2}\right|^2\right)\right.$$
$$\left. + \frac{1}{n_{tes}^2} \sum_{i=1}^{n_{tes}} \sum_{s=1}^{n_{tes}} \prod_{j=1}^{s_{tes}} \left(1 + \frac{1}{2}\left|x_{t,ij} - \frac{1}{2}\right| + \frac{1}{2}\left|x_{t,sj} - \frac{1}{2}\right| - \frac{1}{2}|x_{t,ij} - x_{t,sj}|\right)\right]$$

(41)

where $x_{t,sj}$ denotes the normalized element in the sth row and jth column of the orthogonal table, $x_{t,ij}$ denotes the normalized element in the ith row and jth column of the orthogonal table. According to the properties of orthogonal tables, replacing the levels of columns does not change the orthogonality but does change the homogeneity. Based on this principle and the centered L_2 deviation, the levels of the original orthogonal table columns are replaced to obtain a more uniformly distributed experimental design.

The following STPM is a data-driven reduced-order model whose predictive capability under different working conditions depends on whether the training dataset contains the characteristics of different working conditions. The HU-OTD method is based on the centered L_2 deviation metric to design the working condition parameters such that they more uniformly cover the ranges under study so that the training dataset contains more characteristics of different working conditions.

3.4. Spatial–temporal predictive model

Although the CFD full-dimensional model has high accuracy, the high computational complexity makes it difficult to apply in practice. Moreover, the observation methods are limited, and only sparse data can be collected, making perception of the temperature field of the roaster difficult. To solve these problems, an STPM is proposed, in which a temporal dynamic model is employed to characterize the temporal dynamics of the observation data and a spatial distribution model is employed to characterize the spatial distribution between the observation points and the temperature field. By combining the accurate CFD model provided by the IFC-DA method and the training dataset obtained by the HU-OTD method, the reduced-order model STPM can be constructed, which can achieve fast and accurate prediction of the temperature field based on sparse observation data. The framework of STPM is shown in Fig. 5, which consists of three parts: a temporal dynamic model, a spatial distribution model, and joint spatial–temporal learning.

3.4.1. Temporal dynamic model

The temporal dynamic model is a part of the reduced-order model and is used to describe the dynamic correlation of sparse observation points, thereby realizing prediction of the state of future sparse observation points. $\{\boldsymbol{u}_c, \boldsymbol{y}\}$ represents the collected data, where $\boldsymbol{u}_c \in \mathbf{R}^{L \times n_{in}}$ represents the system input, $\boldsymbol{y} \in \mathbf{R}^{L \times n_{sen}}$ represents the temperature sensor monitoring data, L represents the sampling time, and n_{in} and n_{sen} represent the system input and sensor monitoring dimensions, respectively. The sensor prediction output can be expressed as follows:

$$\hat{\boldsymbol{y}}(t+1) = f^{tem}(\boldsymbol{z}(t)) \quad (42)$$

$$\boldsymbol{z}(t) = [\boldsymbol{u}_c(t), \ldots, \boldsymbol{u}_c(t - l_{in}), \boldsymbol{y}(t), \ldots, \boldsymbol{y}(t - l_{out})] \quad (43)$$

where $f^{tem}(\cdot)$ represents the temporal dynamic model; $\hat{\boldsymbol{y}}(t+1)$ represents the temperature prediction value at time $t+1$; l_{in} and l_{out} represent the time delay labels of the input and output, respectively; and $\boldsymbol{z}(t)$ represents the model input. To form a model training loss function unified with the subsequent spatial distribution model, a neural network model is used to construct the temporal dynamic model, and the expression is as follows:

$$\hat{\boldsymbol{y}}(t+1) = h\left(\boldsymbol{w}^{tem} \cdot \boldsymbol{z}(t) + \boldsymbol{b}^{tem}\right) \cdot \boldsymbol{v}^{tem} + \theta^{tem} \quad (44)$$

where $\boldsymbol{w}^{tem}$ is the weight of the connection of the input layer to the hidden layer in the model, $\boldsymbol{b}^{tem}$ denotes the hidden-layer bias, $\boldsymbol{v}^{tem}$ denotes the connection weight matrix of the hidden layer and the output layer, θ^{tem} denotes the output-layer bias, and $h(\cdot)$ is the activation function. Therefore, Eq. (42) can be expressed as follows:

$$\hat{\boldsymbol{y}}(t+1) = f^{tem}(\boldsymbol{z}(t), \zeta^{tem}) \quad (45)$$

where $\zeta^{tem} = \left[\boldsymbol{w}^{tem}, \boldsymbol{b}^{tem}, \boldsymbol{v}^{tem}, \theta^{tem}\right]^T$ denotes the model parameters, and the loss function of the model (L^{tem}) can be expressed as follows:

$$L^{tem} = \parallel \boldsymbol{y}(t+1) - \hat{\boldsymbol{y}}(t+1) \parallel_2^2$$
$$= \parallel \boldsymbol{y}(t+1) - f^{tem}(\boldsymbol{z}(t), \zeta^{tem}) \parallel_2^2 \quad (46)$$

The above objective function is related only to the model parameters ζ^{tem}, and the optimal parameters can be obtained using the gradient descent optimization method.

3.4.2. Spatial distribution model

The number of temperature sensors is finite, whereas the temperature field is approximately infinite-dimensional. To reconstruct the temperature field from the temperature observation points, a spatial distribution model that maps the low-dimensional temperature observations to the high-dimensional temperature field must be established. Koopman theory proves that a nonlinear system can be mapped to an infinite-dimensional linear system through transformation of the system state and that an infinite-dimensional linear system can be approximated as a finite-dimensional system if a Koopman invariant subspace is found [31], which explains the reasonableness of the construction of the spatial distribution model in this paper. The spatial distribution model is a part of the reduced-order model and is used to establish a mapping relationship between sparse observation points and the entire temperature field so that the entire temperature field can be reconstructed based on the temporal dynamic model prediction and that prediction of the entire temperature field can be realized. The data, $\{\boldsymbol{u}_c, \boldsymbol{y}, \boldsymbol{Y}\}$, are collected, and the system inputs $\boldsymbol{u}_c$ and temperature observation data $\boldsymbol{y}$ are input into the temporal dynamic model to predict the observation temperature $\hat{\boldsymbol{y}}$. $\boldsymbol{Y} \in \mathbf{R}^{L \times n_{fie}}$ denotes the temperature field, which can be obtained from the CFD simulation, and n_{fie} denotes physical
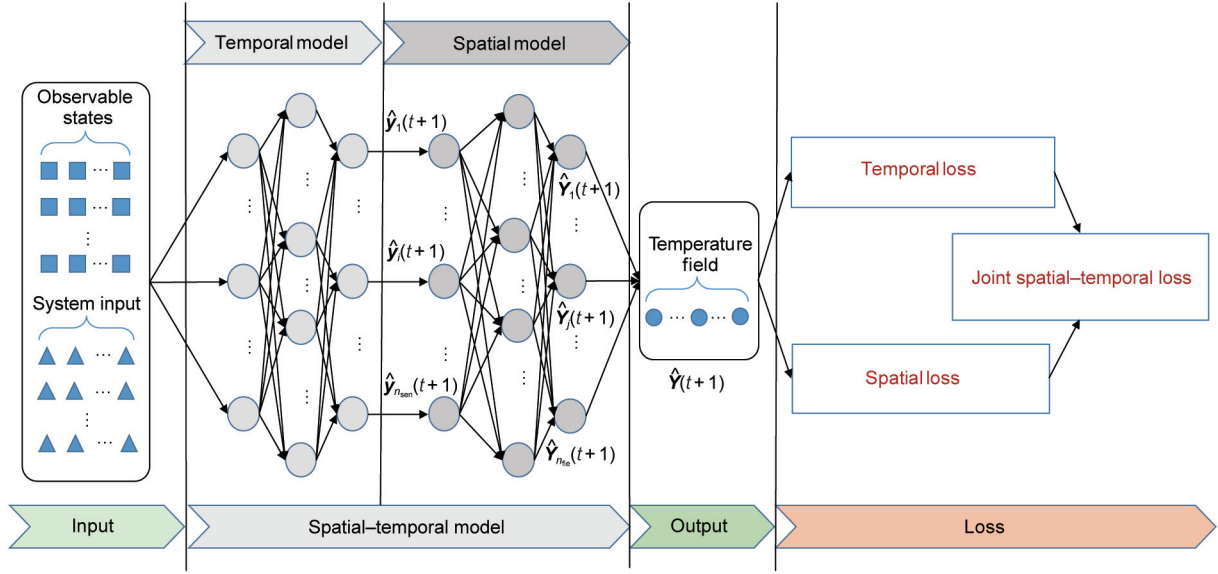
Fig. 5. Framework of STPM.

field dimension. The spatial distribution model can be expressed as follows:

$$\hat{\boldsymbol{Y}}(t+1) = f^{\mathrm{spa}}(\hat{\boldsymbol{y}}(t+1)) \tag{47}$$

where $f^{\mathrm{spa}}(\cdot)$ is the spatial distribution model, which is constructed by a neural network model. $\hat{\boldsymbol{Y}}(t+1)$ denotes the prediction value of the temperature field at time $t+1$. Considering the parameters in the spatial distribution model, Eq. (47) can be transformed as follows:

$$\hat{\boldsymbol{Y}}(t+1) = h(\boldsymbol{w}^{\mathrm{spa}} \cdot \hat{\boldsymbol{y}}(t+1) + \boldsymbol{b}^{\mathrm{spa}}) \cdot \boldsymbol{v}^{\mathrm{spa}} + \theta^{\mathrm{spa}} \tag{48}$$

Similarly, $\zeta^{\mathrm{spa}} = \left[\boldsymbol{w}^{\mathrm{spa}}, \boldsymbol{b}^{\mathrm{spa}}, \boldsymbol{v}^{\mathrm{spa}}, \theta^{\mathrm{spa}} \right]^{\mathrm{T}}$ denotes the parameters of the spatial distribution model. $\boldsymbol{w}^{\mathrm{spa}}$ is the weight of the connection of the input layer to the hidden layer in the model, $\boldsymbol{b}^{\mathrm{spa}}$ denotes the hidden-layer bias, $\boldsymbol{v}^{\mathrm{spa}}$ denotes the connection weight matrix of the hidden layer and the output layer, and θ^{spa} denotes the output-layer bias. Eq. (47) can be expressed as follows:

$$\hat{\boldsymbol{Y}}(t+1) = f^{\mathrm{spa}}(\hat{\boldsymbol{y}}(t+1), \zeta^{\mathrm{spa}}) \tag{49}$$

The loss function for the spatial distribution model (L^{spa}) can be expressed as follows:

$$\begin{aligned} L^{\mathrm{spa}} &= \| \boldsymbol{Y}(t+1) - \hat{\boldsymbol{Y}}(x, t+1) \|_2^2 \\ &= \| \boldsymbol{Y}(t+1) - f^{\mathrm{spa}}\left(\hat{\boldsymbol{Y}}(t+1), \zeta^{\mathrm{spa}} \right) \|_2^2 \end{aligned} \tag{50}$$

Similarly, the objective function Eq. (50) is related only to the spatial distribution model parameters ζ^{spa}, so the optimal parameters of the spatial distribution model can be obtained via the gradient descent method.

3.4.3. Joint spatial–temporal model learning

For the above models, the output of the temporal dynamic model is used as input to the spatial distribution model, which reconstructs the temperature field. To avoid separated learning leading to local optimization of the temporal dynamic and spatial distribution models under their respective learning tasks, which does not lead to global optimization of the spatial–temporal model parameters, these two models must be jointly optimized to obtain the global optimal parameters. The joint learning objective function is as follows:

$$\min_{\zeta^{\mathrm{tem}}, \zeta^{\mathrm{spa}}} \gamma \cdot L^{\mathrm{tem}} + L^{\mathrm{spa}}$$

$$\text{s.t.} \quad \begin{aligned} L^{\mathrm{tem}} &= \| \boldsymbol{y}(t+1) - f^{\mathrm{tem}}(\boldsymbol{z}(t), \zeta^{\mathrm{tem}}) \|_2^2 \\ L^{\mathrm{spa}} &= \| \boldsymbol{Y}(t+1) - f^{\mathrm{spa}}\left(\hat{\boldsymbol{Y}}(t+1), \zeta^{\mathrm{spa}} \right) \|_2^2 \end{aligned} \tag{51}$$

where γ balances the relative contributions of the loss function terms of the temporal dynamic and spatial distribution models. The gradient descent method is applied to optimize Eq. (51). During the optimization process, not only is the impact of parameters ζ^{spa} on the overall model output considered, but also, parameters ζ^{tem} affect the output. The learning process can cause the spatial-temporal model parameters to reach the global optimum.

4. Simulation experiment

To verify the advantages of the proposed method, simulation experiments related to four aspects are set up: the CFD model validation, data assimilation validation, typical working conditions acquisition, and reduced-order model prediction.

CFD model validation: To verify the accuracy of the CFD model, the steady-state and dynamic characteristics of the model and the actual process at 15 observation positions are compared. The steady-state characteristics are evaluated by the mean absolute percentage error (MAPE) and relative error (RE), which are calculated as follows:

$$\mathrm{MAPE} = \frac{1}{L_{\mathrm{sim}}} \times \sum_{f=1}^{L_{\mathrm{sim}}} \frac{|y_{\mathrm{rea}}(x, t_f) - y_{\mathrm{sim}}(x, t_f)|}{y_{\mathrm{sim}}(x, t_f)} \times 100\% \tag{52}$$

$$\mathrm{RE} = \frac{y_{\mathrm{sim}}(x, t_f) - y_{\mathrm{rea}}(x, t_f)}{y_{\mathrm{ref}}} \times 100\% \tag{53}$$

where y_{rea}, y_{sim}, and t_f ($f = 1, \ldots, L_{\mathrm{sim}}$) represent the real value, simulation value, and simulation time, respectively. L_{sim} is total simulation time. $y_{\mathrm{ref}} = 960\,^\circ\mathrm{C}$ is the reference temperature that the roaster works at. To verify the model dynamic characteristics, the Pearson correlation coefficient (r_{p}) is used for evaluation, which is calculated as follows:

$$r_{\mathrm{p}} = \frac{\mathrm{cov}(y_{\mathrm{rea}}(x, t_1 : t_{L_{\mathrm{sim}}}), y_{\mathrm{sim}}(x, t_1 : t_{L_{\mathrm{sim}}}))}{\mathrm{std}(y_{\mathrm{rea}}(x, t_1 : t_{L_{\mathrm{sim}}})) \times \mathrm{std}(y_{\mathrm{sim}}(x, t_1 : t_{L_{\mathrm{sim}}}))} \tag{54}$$

Data assimilation validation: To verify that the proposed method can obtain a more accurate initial physical field, the accuracies of the low-resolution initial physical field and the reconstructed physical field after data assimilation are compared and evaluated via the root-mean-square error (RMSE), which is calculated as follows:

$$\text{RMSE} = \sqrt{\frac{1}{N_{\text{gri}}} \sum_{v=1}^{N_{\text{gri}}} [y_{\text{sim}}(x_v, t_0) - y_{\text{rec}}(x_v, t_0)]^2} \tag{55}$$

where y_{rec}, x_v ($v = 1, \ldots, N_{\text{gri}}$), and t_0 represent the reconstructed value, spatial position of the vth sensor, and initial time, respectively.

Typical working conditions acquisition: To verify the advantages of the proposed method in the acquisition of typical working conditions, the information coverages of the test design before and after improvement are compared and evaluated via the information entropy (H_e), which is calculated as follows:

$$H_e = \sum_{w=1}^{N_{\text{ort}}} p_w \ln p_w / \ln N_{\text{ort}} \tag{56}$$

where p_w denotes the corresponding factor and level test probability.

The calculation of the information entropy metric relies on simulation data under each working condition parameter, which has a high calculation cost. In contrast, the centered L_2 deviation metric only requires the design of the operating condition parameters, avoiding unnecessary CFD simulations. Therefore, the centered L_2 deviation metric is used in the design phase of the design condition parameters, whereas the information entropy metric is used in the validation phase to assess the information content of the dataset.

Reduced-order model prediction: To verify the accuracy and computational efficiency of the reduced-order model, experiments are set up in terms of the prediction performance and extrapolation prediction performance. In the prediction performance experiment, CFD simulations and reduced-order model predictions are compared and evaluated based on the calculation time, RMSE, and MAPE. The extrapolation prediction performance experiment is conducted for unmodeled conditions, in which CFD simulations and reduced-order model predictions are compared and evaluated via RMSE and MAPE.

4.1. CFD model validation

CFD technology is applied to simulate the reaction atmosphere inside the roaster through five steps: geometric model construction, mesh generation, model parameterization, model solution, and model validation. Through comparison with the actual data, the MAPE and r_p of the simulations are calculated to validate the steady-state and dynamic characteristics of the model, respectively. The modeling steps are as follows.

4.1.1. Geometric model construction

According to the actual roaster geometry, as shown in Table 1, the geometric shape of the simulation model is constructed as shown in Fig. 6, where zinc concentrate is thrown in by the ore input, and air is blown in by the air input to form a fluidized reaction environment inside the reactor. After the reaction, the zinc calcine and flue gas are discharged from the calcine and flue gas outputs, respectively. Fifteen temperature sensors are installed on the roaster wall, which are divided into top, middle, and bottom layers according to height, and each layer includes five temperature sensors, that is, A, B, C, D, and E, as shown in Fig. 6. The sensor coordinates are summarized in Table 1.

Table 1
Fluidized bed roaster geometry.

Description	Geometric dimensions
Ore input surface area	0.28 m²
Air input surface area	0.66 m²
Flue gas output surface area	18.00 m²
Calcine output surface area	1.00 m²
R_1	9.56 m
R_2	6.93 m
H_1	4.86 m
H_2	10.93 m
H_3	7.29 m
H_4	5.67 m
H_5	5.37 m
Top layer	$y = 5.0$ m
Middle layer	$y = 2.5$ m
Bottom layer	$y = 0$ m
A	$x = -4.5$ m, $z = -4.5$ m
B	$x = -2.0$ m, $z = 5.5$ m
C	$x = 2.0$ m, $z = 5.5$ m
D	$x = 6.0$ m, $z = 0$ m
E	$x = 4.5$ m, $z = -4.5$ m

4.1.2. Mesh generation

For the CFD calculation, the calculation domain needs to be meshed. Since the shape of the roaster is a nonstandard geometry, the reaction is relatively violent near the feed input and gentle near the output. The free tetrahedral meshing method can be used to divide the mesh size according to the calculation requirements and is suitable for irregular geometries, with a low computational complexity. Therefore, this method is used for meshing in this study.

Theoretically, a smaller mesh size means a higher computational accuracy but increases the rounding error and computational resources. To reasonably perform the meshing, mesh independence verification is needed to verify that the simulation results can converge under different meshing conditions. Therefore, four meshing conditions of 42 000, 84 000, 139 000, and 195 000 meshes are set up, as shown in Figs. 7(a)–(d). The simulation results of 15 temperature sensors under these four meshing conditions are compared, as shown in Fig. 7(e). The results for 42 000 meshes significantly deviate, whereas the results for the other three meshes are similar. Considering the model accuracy and computational complexity, the division method of 139 000 meshes is selected.

4.1.3. Model parameterization

To simulate the reaction atmosphere of the roaster, the boundary conditions must be set according to its actual operation, which include air and ore input boundary conditions. The feed components and speed affect the ore input boundary conditions, and three different feed components are considered, as shown in Table 2. For the steady-state simulation, the feed speed is 37.35 t·h⁻¹, and the blast speed is 63 266.46 m³·h⁻¹ for 100 min. For the dynamic simulation, the feed and blast speeds are 43.29 t·h⁻¹ and 63 555.93 m³·h⁻¹ at 0–100 min, respectively, and the slopes change to 41.87 t·h⁻¹ and 67 736.91 m³·h⁻¹ at 100–200 min and then remain unchanged at 200–300 min.

4.1.4. Model solution

After the model structure and parameters are specified, the model is solved by the sequential solution method, which is implemented using the transient solver in COMSOL Multiphysics. The solution step size, output step size, relative tolerance of the solution, and solution time for steady-state and dynamic verification are set as 0.01 min, 0.1 min, 0.05, 100 min, and 300 min, respectively.
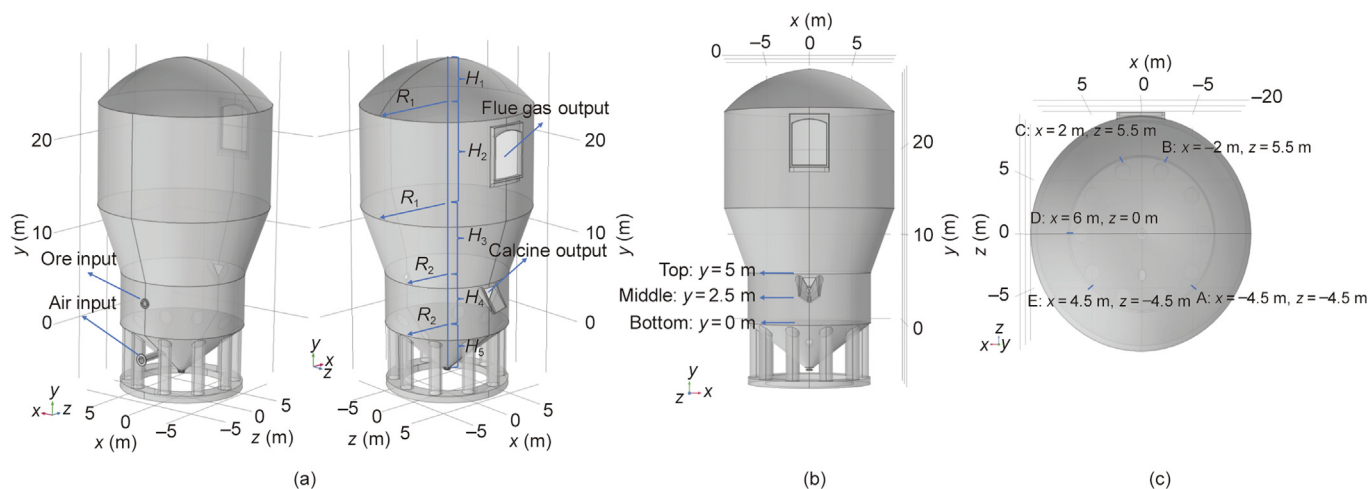
Fig. 6. Fluidized bed roaster geometry model: (a) stereo view, (b) front view, and (c) top view.
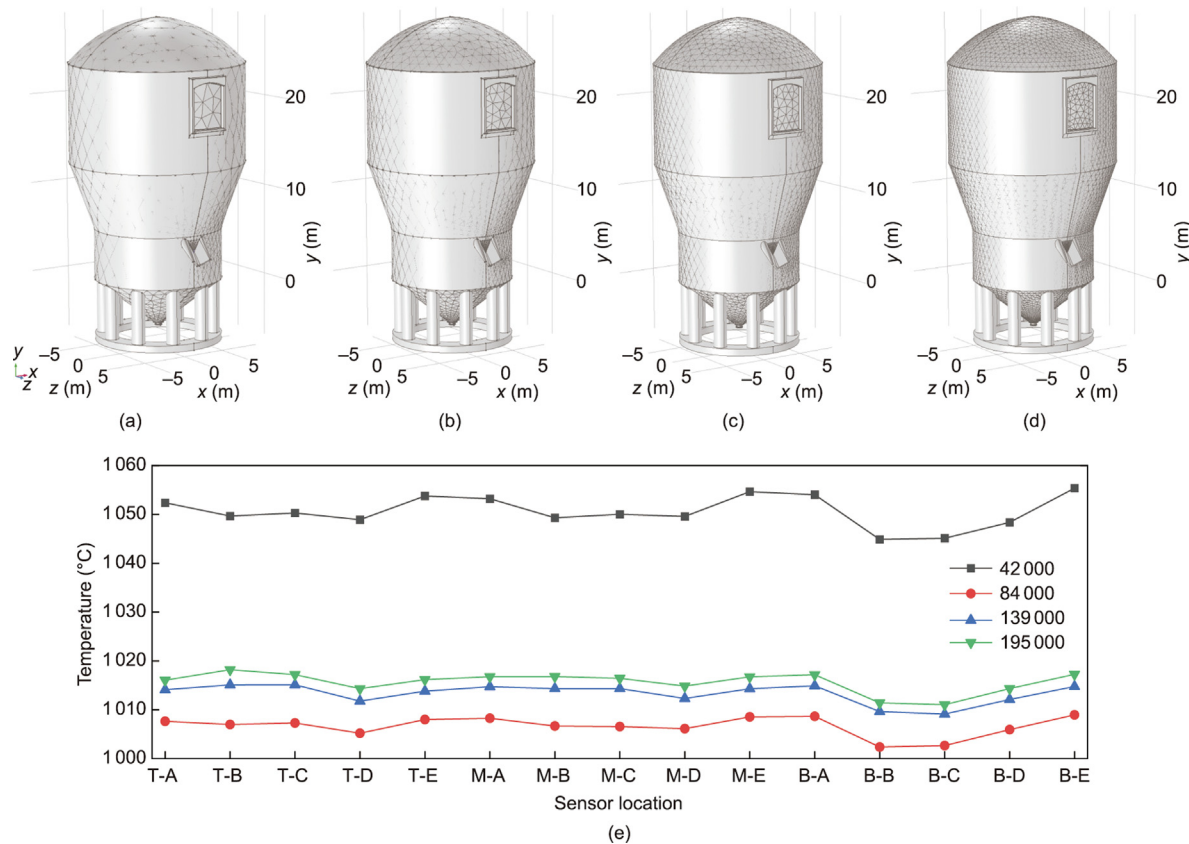

Fig. 7. Mesh generation: (a) 42 000, (b) 84 000, (c) 139 000, and (d) 195 000. (e) Comparison of simulation results for different meshing conditions. T, M, and B denote top, middle, and bottom layers, respectively.

Table 2
Feed component test results.

Component	Content (%)					
	Zn	Fe	Pb	SiO$_2$	S	Cu
1	46.04	11.51	1.27	1.88	29.83	0.61
2	47.67	9.32	1.28	1.93	29.33	0.79
3	49.43	8.05	1.75	2.67	31.23	0.91

4.1.5. Model validation

To verify the accuracy of the CFD model, real and simulation data at 15 observation locations are compared in terms of both steady-state and dynamic characteristics. Steady-state characteristics verification considers three different components and uses MAPE and RE for evaluation. Dynamic characteristics verification considers only component 1 and adopts r_p for evaluation. The verification results are as follows.

Steady-state characteristics verification: Figs. 8(a)–(c) show the RE between the simulation and the actual value for component 1. The REs at positions A, B, and D remain within [−0.01%, 0.02%], indicating a good steady-state fitting effect, whereas the deviations at positions C and E are slightly larger. The main reason is that the model assumes that the roaster is a regular reactor, but owing to the aging of the roaster body and the sintering fault, the ore is enriched in some locations, resulting in higher temperatures. To reflect the generalization performance of the model simulation, the MAPEs under three different components are calculated, as shown in Fig. 8(d), and they are all maintained under 7%. Therefore, the constructed CFD model has good steady-state simulation performance and can accurately simulate the steady-state characteristics of the roaster under different components.

Dynamic characteristics verification: Fig. 9 shows the dynamic verification of the model. The simulation and actual curves are in good agreement, and both have a downward trend at 150 min. The main reason is that the feed and blast speed slopes change at 100–200 min. A greater wind speed results in more heat being removed, and a reduced feed speed will lower the reaction heat, decreasing the temperature. To quantify the dynamic simulation effect of the model, the r_p values of the simulation are calculated, and the average value exceeds 0.9. Therefore, the constructed model can simulate the dynamic influence of feed and blast on the temperature field well and has good dynamic simulation performance.

4.2. Data assimilation validation

The initial physical field affects the accuracy of the CFD simulation. Minor initial errors will lead to large simulation deviations after multiple iterations. Traditional methods usually obtain low-resolution initial physical fields through benchmark models, which are inconsistent with actual sparse observations. To solve this problem, this paper proposes an IFC-DA method. The experiment used to verify the accuracy of the reconstructed initial field is designed as follows:

(1) Data collection: The data include mainly sparse observation data and a low-resolution background field. The sparse observation data are categorized into four cases: 64×12, 32×6, 21×4, 16×3, and the sparse data are uniformly distributed in the temperature field, as shown in Fig. 10(a). The background field dimensions are 320×60, and the resolution is 0.1 m $\times$ 0.1 m, as shown in Fig. 10(b).

(2) 3D variational data assimilation: Based on the low-resolution background field and sparse observation data, the objective function shown in Eq. (36) is constructed, and the reconstructed physical field is obtained through optimization and uniform filtering.

(3) Evaluation of the reconstructed initial field accuracy: The RMSEs between the real physical field and background field, as well as between the real physical field and the reconstructed physical field, are calculated and compared. The real physical field dimensions are 640×120, and the resolution is 0.05 m $\times$ 0.05 m.
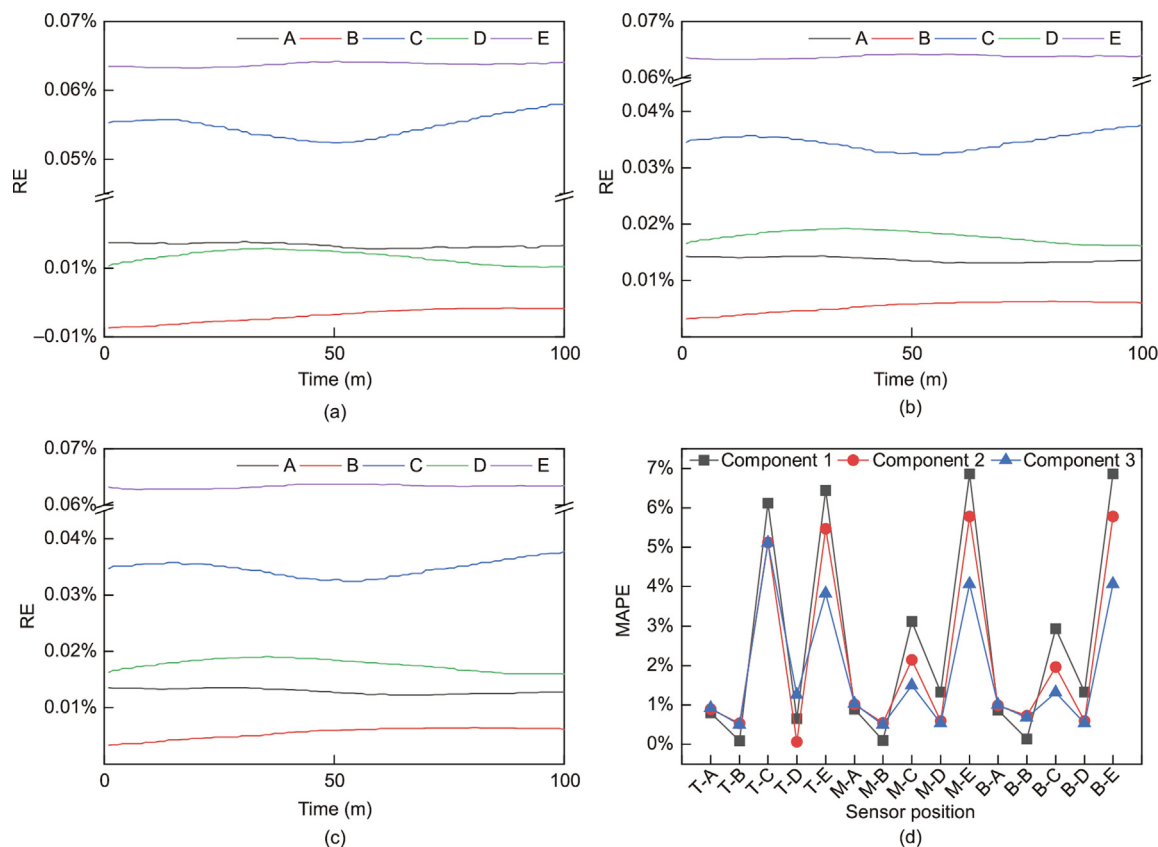

Fig. 8. Verification of the steady-state characteristics of the model. (a–c) Model simulation deviations in the (a) top, (b) middle, and (c) bottom layers for component 1. (d) Model steady-state simulation effect.
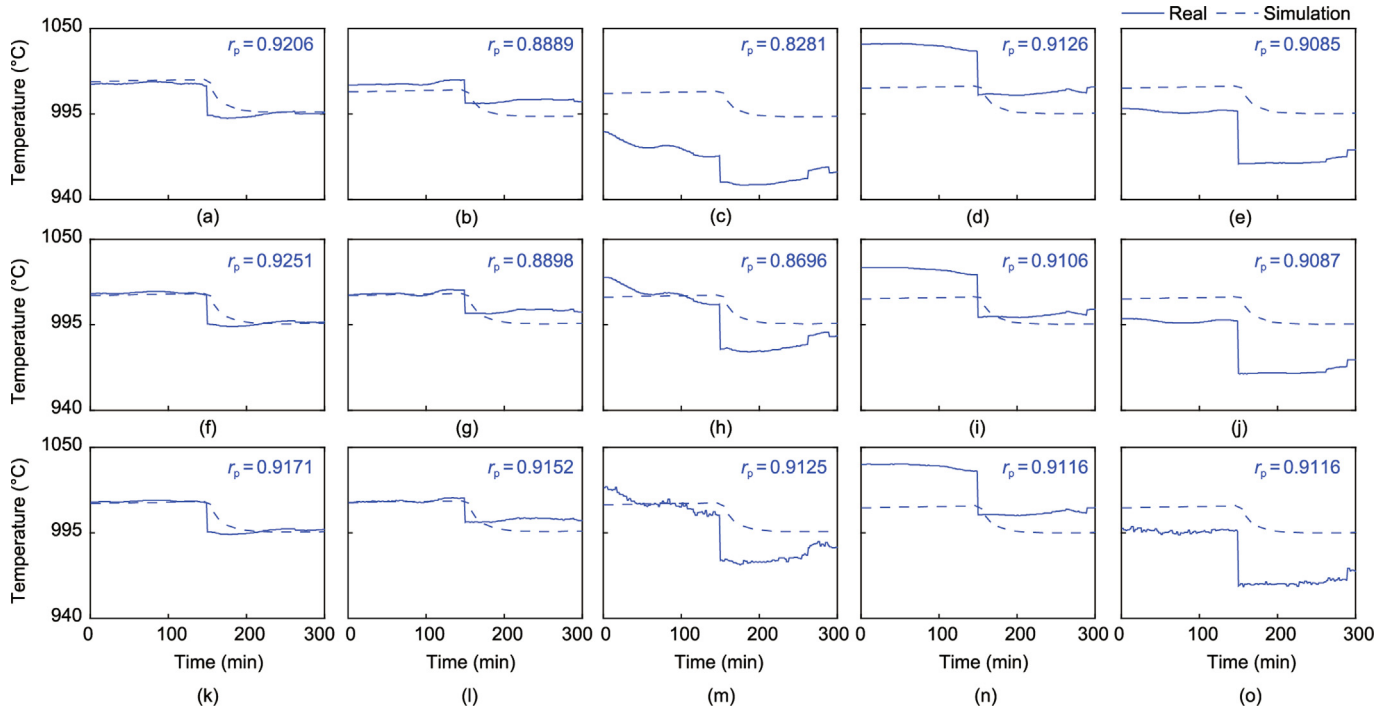
Fig. 9. Comparison of actual data and simulation results: (a–e) top layer A–E; (f–j) middle layer A–E; and (k–o) bottom layer A–E.
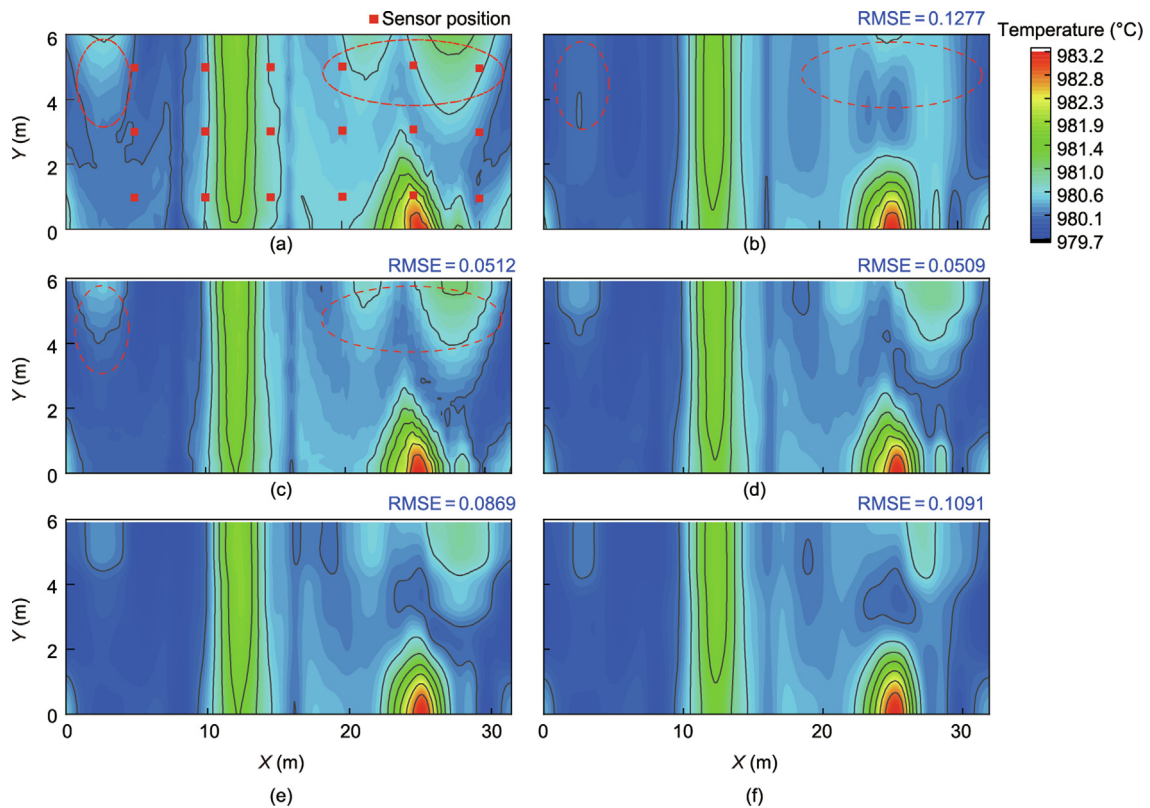

Fig. 10. Initial physical field reconstruction effect. (a) Real physical field (0.05 m × 0.05 m). (b) Low-resolution background field (0.1 m × 0.1 m). (c–f) Reconstruction of the physical field based on (c) 64 × 12, (d) 32 × 6, (e) 21 × 4, and (f) 16 × 3 sparse data (0.05 m × 0.05 m).

The low-resolution background field reaches the same resolution as the real physical field through linear interpolation for comparison.

Fig. 10 shows the effect of the proposed method on data assimilation. A comparison of the contents of the red dotted circles in

Figs. 10(a) and (b) reveal that the details of the background field are not accurate. The main reason is that the preliminary simulation can be carried out only based on low-resolution meshes, so the marginal details of the temperature field cannot be fully reflected. Figs. 10(c)–(f) show the temperature field after data

assimilation. Through the correction of sparse data, the temperature field can be reconstructed with a higher accuracy based on the background field, and its detailed characteristics can be reflected. The RMSEs are calculated to quantify the data assimilation effect. As the amount of sparse data increases, RMSE gradually decreases. When the sparse data reach dimensions of 32×6, the RMSE no longer decreases. The main reason is that although more sparse data can provide more accurate information for data assimilation such that the reconstructed temperature field will be more precise, the information provided by 32×6 dimension sparse data reaches the upper limit, and the addition of more sparse data cannot significantly improve the reconstruction effect. However, generally, the accuracy of the temperature field after data assimilation is better than that of the low-resolution background field.

4.3. Typical working condition acquisition

There are many working conditions in the temperature field of the roaster, and comprehensive CFD simulations are costly. The traditional OTD method does not adequately cover the parameter ranges. To reduce simulation costs and cover the ranges, this paper proposes an HU-OTD method. The experiment used to verify the advantages of the proposed method in the acquisition of typical working conditions is designed as follows:

(1) OTD: The temperature field of the roaster is affected mainly by the components (zinc content), feed speed, and blast speed, which are in the ranges of 45%–50%, 35–40 t·h^{-1}, and 6×10^4– 7×10^4 m^3·h^{-1}. Each factor is divided into three levels, and the test is designed using the $L_9(3^4)$ orthogonal table.

(2) Introduction of the centered L_2 deviation for improvement: Based on the table, the levels of columns are replaced by minimizing Eq. (41) to design working condition parameters with high uniformity.

(3) Evaluation of the amount of working condition information: The temperatures at four locations in the roaster center, that is, (−2.5, 5.0, −2.0), (2.5, 5.0, −2.0), (−2.5, 5.0, 2.0), and (2.5, 5.0, 2.0), are used to calculate H_e to evaluate the amount of working condition information.

Table 3 shows the effectiveness of the proposed method in obtaining typical working conditions data. The difference between the HU-OTD and OTD methods is the replacement of 35 and 40 levels of the feed speed factor, but the corresponding centered L_2 deviation is reduced from 0.03319 to 0.03303, which indicates that the proposed method can design parameters that are more uniformly distributed. To precisely quantify the amount of informa-

tion contained in the designed conditions, the values of H_e of the working conditions data are calculated. The H_e of HU-OTD is significantly greater than that of OTD, and it is increased by 6% or more (Table 4); thus, the working condition parameters set by the HU-OTD method can more fully cover the parameter ranges, and the typical working conditions data obtained at the same test cost contain more information.

4.4. Reduced-order model prediction

Although the full-dimensional CFD model can comprehensively and accurately describe the temperature field in the roaster, this model has a high computational complexity and is difficult to apply in practice. To solve this problem, an STPM is proposed, which can quickly and accurately predict the temperature field based on sparse observation data. To verify the accuracy and computational efficiency of STPM, prediction experiments are set up. First, STPM is obtained using the joint learning framework through the acquired typical working condition data. Then, STPM is used to predict the test data of the modeled working conditions and is compared with CFD simulations to determine the accuracy and calculation efficiency of the model. Finally, STPM is used to predict unmodeled working condition data and is compared with the CFD model to show that the model also has a good extrapolation prediction effect for unmodeled conditions.

4.4.1. Predictive model development

STPM construction includes two steps: dataset construction and joint spatial–temporal learning.

(1) Dataset construction: According to the nine working conditions set based on the HU-OTD method in Table 3, each working condition is simulated for 101 min, and the sampling interval is 1 min. A total of 909 datasets are obtained. The 15-dimensional temperature observation data and working condition parameters at the current time and the 125-dimensional temperature field state inside the roaster at the next time constitute the data pairs, with a total of 900 data pairs, of which 70% (630 pairs) are randomly selected as the training data. All the data pairs are used as the test data.

(2) Joint spatial–temporal learning: To address the problem that the separated learning method will make the model parameters locally optimal, the optimal parameters of STPM are obtained via the joint learning method. First, the temporal dynamic and spatial distribution model structures are set up according to the temperature observations and field dimensions. Then, the two sub-models

Table 3
Comparison of test designs.

Method	Condition	Zn content (%)	Feed speed (t·h^{-1})	Blast speed (m^3·h^{-1})	Temperature (°C)			
					(−2.5, 5.0, −2.0)	(2.5, 5.0, −2.0)	(−2.5, 5.0, 2.0)	(2.5, 5.0, 2.0)
OTD	1	45.00	35.00	60 000	996.2318	995.9756	995.5182	994.8459
	2	45.00	40.00	65 000	992.6284	992.4662	991.9648	991.6991
	3	45.00	45.00	70 000	993.6535	993.1024	993.0029	992.1115
	4	47.50	35.00	65 000	991.6736	991.5238	991.0611	990.8158
	5	47.50	40.00	70 000	992.5126	992.0251	991.9202	991.1371
	6	47.50	45.00	60 000	1 002.5561	1 002.2147	1 001.5472	1 000.6452
	7	50.00	35.00	70 000	991.3829	990.9345	990.8369	990.1165
	8	50.00	40.00	60 000	1 000.4215	1 000.1012	999.4731	998.6265
	9	50.00	45.00	65 000	996.6403	996.4364	995.8164	995.4823
HU-OTD	1	45.00	40.00	60 000	998.9809	998.6924	998.1322	997.3751
	2	45.00	35.00	65 000	991.2349	991.0942	990.6550	990.4232
	3	45.00	45.00	70 000	993.9101	993.5969	993.2274	992.7357
	4	47.50	40.00	65 000	993.4673	993.2962	992.7673	992.4871
	5	47.50	35.00	70 000	990.7670	990.5106	990.2080	989.8055
	6	47.50	45.00	60 000	1 002.6891	1 002.3492	1 001.6810	1 000.7804
	7	50.00	40.00	70 000	993.6140	993.3049	992.9405	992.4553
	8	50.00	30.00	60 000	997.8133	997.5343	996.9902	996.2550
	9	50.00	45.00	65 000	996.4249	996.2217	995.5909	995.2581

Table 4

Comparison of the H_e of temperatures at the four locations.

Method	H_e			
	(−2.5, 5.0, −2.0)	(2.5, 5.0, −2.0)	(−2.5, 5.0, 2.0)	(2.5, 5.0, 2.0)
OTD	0.7802	0.7935	0.7764	0.8011
HU-OTD	0.8416	0.8453	0.8408	0.8499

Table 5

STPM extrapolation prediction performance.

Condition	Zn content (%)	Feed speed (t·h^{-1})	Blast speed (m^3·h^{-1})	RMSE	MAPE (%)
1	45.0	40	67 500	0.0970	0.0078
2	47.5	37	65 000	0.0353	0.0023
3	49.0	35	70 000	0.0410	0.0032
4	49.0	37	67 500	0.1089	0.0095

are pre-trained to obtain the initial parameters. Finally, the two sub-models are jointly optimized. The neural networks are trained using the Adam solver with a learning rate of 0.01, 10 000 pre-training iterations, and 5000 joint training iterations.

4.4.2. Prediction performance

To verify the prediction performance of STPM, a prediction performance experiment is conducted. The 15-dimensional temperature observation data and working condition parameters at the current time are input into STPM to predict the temperature field of the roaster at the next time and to predict 100 steps in sequence. The predicted and simulated temperature fields are compared in terms of RMSE, MAPE, and the calculation time.

Compared with the simulation results of the CFD model, RMSE and MAPE are maintained at a low level, indicating that STPM has good prediction performance, and STPM only needs a 0.1176 s prediction time, which is much shorter than the 4020 s prediction time of the CFD model. The main reason is that the typical working conditions data obtained by the HU-OTD method contain the operating characteristics of the temperature field of the roaster, and STPM learns the distribution and dynamic characteristics through the spatial distribution and temporal dynamic models, respectively. The joint learning method is used to optimize the overall model parameters, which can characterize the operating characteristics of the roaster temperature field well. In addition, the iterative learning process with a high computational complexity is completed in the offline stage. Only simple neural network derivation calculations are required in the online stage, which only requires a short prediction time. Therefore, the proposed STPM can significantly reduce the calculation time required for online prediction with high accuracy, and the calculation efficiency is improved by 3.4184×10^4 times.

4.4.3. Extrapolation prediction performance

To verify the extrapolation prediction performance of STPM, an extrapolation prediction effect experiment is set up, and four working conditions that are not in HU-OTD are set, as shown in Table 5. The predictions of STPM and the CFD model are compared and evaluated via RMSE and MAPE.

Table 5 summarizes the extrapolation prediction effect of STPM. Although STPM does not learn the data characteristics of the extrapolation working conditions during the training process, it still has good prediction performance. The main reason is that these extrapolation working condition parameters are within the studied parameter ranges, and the working condition parameters designed by HU-OTD can fully cover the ranges. In addition, STPM is constructed by neural networks with a certain extrapolation performance, so it also has good prediction performance for unmodeled conditions. Compared with the modeled conditions, STPM

predicts the unmodeled conditions with maximum reductions of 0.0709 in RMSE and 0.0070% in MAPE, maintaining a high prediction accuracy. Therefore, the proposed STPM can be concluded to also have good extrapolation prediction performance for unmodeled conditions.

5. Conclusions

The zinc fluidized bed roaster is a typical process manufacturing system, and its internal temperature field information is essential. However, realizing real-time and accurate perception of the temperature field is difficult because of limited sensing methods and complex coupled reaction atmospheres. To solve this problem, a STROM is proposed in this paper. First, to address the problem that the initial physical field and sparse observation data are difficult to match, an IFC-DA method is proposed to realize reconstruction of the high-resolution initial physical field. To address the high cost of comprehensive CFD simulations of multiple working conditions, an HU-OTD method in which the centered L_2 deviation is introduced is proposed, which achieves full coverage of the parameter ranges. Finally, to address the difficulty of real-time accurate perception of the temperature field, an STPM is proposed. Extensive experiments show that the proposed method has three major advantages: ① High-precision and high-resolution model initial conditions are reconstructed based on sparse observations and a low-resolution background field; ② tests can be designed so that the condition characteristics adequately cover the parameter ranges at a small simulation cost; and ③ the accuracy of temperature field perception can be guaranteed while the simulation computation efficiency can be greatly improved. However, the performance of STPM depends on data quality, and the model output does not fully meet the physical constraints. In future research, it is necessary to integrate the mechanism knowledge in CFD into the model framework to improve the prediction performance.

CRediT authorship contribution statement

Yunfeng Zhang: Writing – original draft, Methodology, Data curation. **Chunhua Yang:** Software, Methodology, Conceptualization. **Keke Huang:** Writing – review & editing, Methodology, Conceptualization. **Tingwen Huang:** Writing – review & editing, Methodology. **Weihua Gui:** Writing – review & editing, Methodology.

Declaration of competing interest

The authors declare that they have no known competing financial interests or personal relationships that could have appeared to influence the work reported in this paper.

Acknowledgments

References

[1] Yu W, Wu M, Huang B, Lu C. A generalized probabilistic monitoring model with both random and sequential data. Automatica 2022;144:110468.

[2] Meng X, Liu Q, Yang C, Zhou L, Cheung YM. A novel deep learning-based robust dual-rate dynamic data modeling for quality prediction. IEEE Trans Industr Inform 2024;20(2):1324–34.

[3] Zhu T, Liu X, Wang X, He H. Technical development and prospect for collaborative reduction of pollution and carbon emissions from iron and steel industry in China. Engineering 2023;31:37–49.

[4] Wei K, Huang K, Yang C, Gui W. Multi-objective adaptive optimization model predictive control: decreasing carbon emissions from a zinc oxide rotary kiln. Engineering 2023;27:96–105.

[5] Bao Y, Zhu Y, Qian F. A local quadratic embedding learning algorithm and applications for soft sensing. Engineering 2022;18:186–96.

[6] Mao S, Wang B, Tang Y, Qian F. Opportunities and challenges of artificial intelligence for green manufacturing in the process industry. Engineering 2019;5(6):995–1002.

[7] Wang X, Zhao H. A high-efficiency two-stroke engine concept: the boosted uniflow scavenged direct-injection gasoline (BUSDIG) engine with air hybrid operation. Engineering 2019;5(3):535–47. Erratum in: Engineering 2019;5 (5):979.

[8] Wang S, Luo K, Hu C, Fan J. CFD-DEM study of the effect of ring baffles on system performance of a full-loop circulating fluidized bed. Chem Eng Sci 2019;196:130–44. Erratum in: Chem Eng Sci 2020;216:115590.

[9] Wu Y, Liu D, Zheng D, Ma J, Duan L, Chen X. Numerical simulation of circulating fluidized bed oxy-fuel combustion with dense discrete phase model. Fuel Process Technol 2019;195:106129.

[10] Hu C, Luo K, Wang S, Sun L, Fan J. Influences of operating parameters on the fluidized bed coal gasification process: a coarse-grained CFD-DEM study. Chem Eng Sci 2019;195:693–706.

[11] Liu D, Song J, Ma J, Chen X, van Wachem B. Gas flow distribution and solid dynamics in a thin rectangular pressurized fluidized bed using CFD-DEM simulation. Powder Technol 2020;373:369–83.

[12] Hou B, Wang X, Zhang T, Li H. A model for improving the Euler–Euler two-phase flow theory to predict chemical reactions in circulating fluidized beds. Powder Technol 2017;321:13–30.

[13] Cardoso J, Silva V, Eusébio D, Brito P, Tarelho L. Improved numerical approaches to predict hydrodynamics in a pilot-scale bubbling fluidized bed biomass reactor: a numerical study with experimental validation. Energy Convers Manage 2018;156:53–67.

[14] Pang B, Wang S, Chen W, Hassan M, Lu H. Effects of flow behavior index and consistency coefficient on hydrodynamics of power-law fluids and particles in fluidized beds. Powder Technol 2020;366:249–60.

[15] Dash S, Mohanty S, Mishra BK. CFD modelling and simulation of an industrial scale continuous fluidized bed roaster. Adv Powder Technol 2020;31 (2):658–69.

[16] Wu Y, Liu D, Duan L, Ma J, Xiong J, Chen X. Three-dimensional CFD simulation of oxy-fuel combustion in a circulating fluidized bed with warm flue gas recycle. Fuel 2018;216:596–611.

[17] Feng Y, Wang Y, Wang BC, Li HX. Spatial decomposition-based fault detection framework for parabolic-distributed parameter processes. IEEE Trans Cybern 2022;52(8):7319–27.

[18] Alam K, Ray T, Anavatti SG. Design optimization of an unmanned underwater vehicle using low- and high-fidelity models. IEEE Trans Syst Man Cybern Syst 2017;47(11):2794–808.

[19] Wang JW, Li HX, Wu HN. A membership-function-dependent approach to design fuzzy pointwise state feedback controller for nonlinear parabolic distributed parameter systems with spatially discrete actuators. IEEE Trans Syst Man Cybern Syst 2017;47(7):1486–99.

[20] Saberian A, Sajadiye SM. Assessing the variable performance of fan-and-pad cooling in a subtropical desert greenhouse. Appl Therm Eng 2020;179:115672.

[21] Yu J, Lu L, Gao X, Xu Y, Shahnam M, Rogers WA. Coupling reduced-order modeling and coarse-grained CFD-DEM to accelerate coal gasifier simulation and optimization. AIChE J 2021;67(1):e17030.

[22] Xie W, Bonis I, Theodoropoulos C. Data-driven model reduction-based nonlinear MPC for large-scale distributed parameter systems. J Process Contr 2015;35:50–8.

[23] Du C, Han C, Yang Z, Wu H, Luo H, Niedzwiecki L, et al. Multiscale CFD simulation of an industrial diameter-transformed fluidized bed reactor with artificial neural network analysis of EMMS drag markers. Ind Eng Chem Res 2022;61(24):8566–80.

[24] Qian F. Smart process manufacturing toward carbon neutrality: digital transformation in process manufacturing for achieving the goals of carbon peak and carbon neutrality. Engineering 2023;27:1–2.

[25] Zheng D, Zhou L, Song Z. Kernel generalization of multi-rate probabilistic principal component analysis for fault detection in nonlinear process. IEEE/CAA J Autom Sin 2021;8(8):1465–76.

[26] Qing X, Jin J, Niu Y, Zhao S. Time–space coupled learning method for model reduction of distributed parameter systems with encoder–decoder and RNN. AIChE J 2020;66(8):e16251.

[27] Lorenzetti J, McClellan A, Farhat C, Pavone M. Linear reduced-order model predictive control. IEEE Trans Automat Contr 2022;67(11):5980–95.

[28] Wu Y, Liu D, Ma J, Chen X. Effects of gas–solid drag model on Eulerian–Eulerian CFD simulation of coal combustion in a circulating fluidized bed. Powder Technol 2018;324:48–61.

[29] Wu Y, Liu D, Hu J, Ma J, Chen X. Comparative study of two fluid model and dense discrete phase model for simulations of gas–solid hydrodynamics in circulating fluidized beds. Particuology 2021;55:108–17.

[30] Liu D, Xia S, Tang H, Zhong D, Wang B, Cai X, et al. Parameter optimization of PEMFC stack under steady working condition using orthogonal experimental design. Int J Energy Res 2019;43(7):2571–82.

[31] Koopman BO. Hamiltonian systems and transformation in Hilbert space. Proc Natl Acad Sci USA 1931;17(5):315–8.